



OPEN

Time dependent seismic fragility and serviceability assessment of reinforced concrete frames under chloride induced corrosion

Behrouz Kordtabar¹, Mehdi Dehestani¹✉, Omid Yazdanpanah² & Aref Hasanzadeh¹

Chloride-induced corrosion represents a critical deterioration mechanism for reinforced concrete (RC) structures, yet its time-dependent impact on structural reliability remains insufficiently investigated. This study integrates a corrosion progression model with finite element analysis and the First-Order Reliability Method (FORM) to evaluate the seismic performance and serviceability of a single-bay, single-story RC frame throughout a 60-year service life. Nonlinear dynamic, static, and modal analyses were conducted using OpenSees and MATLAB to quantify failure probabilities for both drift-based seismic damage states and serviceability criteria (deflection and vibration). The results demonstrate that corrosion significantly amplifies failure risk: for slight, moderate, and extensive seismic damage states, failure probability increases by approximately 46–56%, 52–55%, and 34–47%, respectively, compared to an uncorroded frame. Serviceability reliability similarly deteriorates, with corrosion raising the probability of deflection and floor vibration failure by approximately 30–37% over the 60-year period. A sensitivity analysis identified the corrosion initiation time, chloride diffusion coefficient, and rebar diameter as governing uncertainties affecting the reliability index. Notably, the influence of corrosion-model parameters (such as time to initiation) on reliability is pronounced during early years but diminishes at later stages of the service life. These findings highlight the significant long-term vulnerability of RC frames in chloride-rich environments and underscore the value of probabilistic approaches for assessing structural resilience under progressive corrosive deterioration.

Keywords Corrosion failure, Reliability analysis, Reinforced concrete frame, Lateral displacement, Serviceability

The development of reinforced concrete (RC) structures for economic, social, and urban purposes in corrosive environments remains unavoidable. Consequently, structural damage in such conditions presents a realistic concern. Various deterioration mechanisms, including fatigue, abrasion, carbonation, and chloride-induced corrosion, affect these structures^{1–5}. Among these mechanisms, chloride-induced corrosion causes the most severe degradation^{6–9}. Previous studies demonstrate that chloride ions gradually penetrate the concrete cover and, upon reaching the steel reinforcement surface, initiate rust formation. The volumetric expansion associated with rust production leads to concrete cover cracking. Chloride-induced corrosion, coupled with reinforcement mass reduction^{10,11}, diminishes the mechanical properties of both steel reinforcement¹² and surrounding concrete cover¹³. Research findings reveal that corrosion significantly contributes to structural capacity reduction. In corrosion-prone environments, RC structures become more vulnerable to damage and exhibit increased susceptibility to natural hazards such as earthquakes during their service life^{14–19}. Therefore, investigating corrosion impacts on seismic performance of RC structures over time remains essential.

Previous investigations into chloride-induced corrosion effects on RC structures fall into three main categories. The first category focuses on corrosion impacts on individual RC material properties, such as steel reinforcement and concrete. These studies subjected carefully prepared reinforced and unreinforced laboratory specimens to various corrosion conditions. These investigations examined chloride ion penetration depth and reinforcement corrosion, providing empirical relationships describing the correlation between chloride-induced

¹Faculty of Civil Engineering, Babol Noshirvani University of Technology, Babol, Iran. ²Hybrid Structural Testing Center (Core Research Center for Smart Infrastructure), Myongji University, Yongin-si, Republic of Korea. ✉email: dehestani@nit.ac.ir

corrosion, reinforcement mass loss, and material mechanical property deterioration. Both theoretical and empirical models have been employed to achieve comprehensive understanding of these effects^{12,20–23}.

The second category addresses corrosion influence on structural performance of RC members, including beams and columns. Combined numerical and experimental analyses assessed corrosion-induced material degradation effects on reinforcement bond-slip behavior^{24–26} and flexural and shear performance of beams and columns^{27–30}. Results indicate that corrosion significantly affects performance and failure modes of RC structural members^{31–35}.

The third category pertains to seismic performance assessment of corrosion-damaged RC structures^{36,37}. This research primarily focused on vulnerability of bridges and buildings where steel reinforcement underwent uniform corrosion within concrete. Time-dependent corrosion models predicted deterioration progression, while structural responses underwent evaluation through pushover or dynamic analyses. Damage indices included interstory drift, relative rotation, base shear, and other parameters.

Earlier studies treated structural parameters and corrosion models deterministically. Although valuable research has examined probabilistic assessments of corrosion effects on RC structures^{38–41}, further advancement of probabilistic methodologies in this field remains necessary. Field investigations on RC structures demonstrate considerable uncertainty in estimating corrosion initiation models^{42–44}. This uncertainty in corrosion parameters and models, combined with earthquake occurrence unpredictability, emphasizes the necessity for probabilistic analysis. Failure probability estimation without probabilistic methods may produce overly conservative results.

Recent advances in structural engineering have focused on improving seismic performance through optimizing cross-sectional parameters, utilizing advanced materials, developing prefabricated connections, and applying sophisticated numerical modeling techniques. These innovations directly inform the analytical approach adopted in this study, particularly in modeling nonlinear behavior and deterioration mechanisms under cyclic loading. For example, advanced numerical methods enable more accurate representation of bond-slip and material degradation phenomena critical to evaluating seismic resilience^{47–50}. Similarly, optimization of material properties and section details enhances the reliability and ductility of reinforced concrete elements, which underpins the modeling of corroded RC frames considered here^{45,46,51,52}. Thus, this study builds upon these trends by integrating material degradation and nonlinear response within a probabilistic framework to assess structural performance over service life.

This study investigates chloride-induced corrosion effects on RC frames, focusing on reinforcement and concrete material deterioration over a 60-year period. The research employs corrosion modeling coupled with finite element analysis using OpenSees software to predict nonlinear behavior and potential structural failures. RC frame failure probability undergoes evaluation via reliability analysis considering corrosion parameter uncertainties and performance-based criteria, with drift used as the performance indicator. Based on previous studies and investigations, To our knowledge, this is the first study to comprehensive assessment of time-dependent chloride corrosion effects on RC frame seismic performance, utilizing finite element modeling within a reliability and uncertainty framework.

Methodology

Corrosion model

Deterioration models due to chloride ions attack

To predict the service life of RC structures in corrosive environments where chloride ions predominantly contribute to deterioration, it is essential to utilize useful life prediction models related to the same area. The general equation for estimating the penetration depth of chloride ions, which is subject to Fick's second law through diffusion theory, is expressed as Eq. (1)^{53,54}:

$$C(x, t) = C_s \left[1 - \operatorname{erf} \left(\frac{x}{2\sqrt{Dt}} \right) \right] \quad (1)$$

where $C(x, t)$ and D stand for the chloride ion concentration at depth x and time t , and the chloride diffusion coefficient, respectively. $\operatorname{erf}(\cdot)$ is the error function. Corrosion initiation occurs when the chloride concentration within the depth of the cover concrete reaches the specified threshold level. Therefore, by taking place C_b and C_{cr} , respectively, instead of x and $C(x, t)$ in Eq. (1), the corrosion initiation, T_{init} , is expressed as Eq. (2):

$$T_{init} = \left\{ \frac{C_b^2}{4D} \left[\operatorname{erf}^{-1} \left(1 - \frac{C_{cr}}{C_s} \right) \right]^{-2} \right\} \quad (2)$$

In practical conditions, parameters such as water to cement, relative humidity, the size of the cover concrete crack, and the bonding of chloride ions play a significant role in the diffusion coefficient⁵⁵. In this study, only the effect of cracking on the chloride diffusion coefficient is considered as $D = D_{ref} f(w)$, where D_{ref} is the reference chloride diffusion coefficient at 28 days, depending on the water-cement ratio (w/c). Empirical Eq. (3)⁵⁶ expresses this coefficient in terms of (m^2/s) for ordinary concrete.

$$D_{ref} = 10^{-12.06+2.4 w/c} \quad (3)$$

Hairline cracks can occur in concrete after concrete placing due to various reasons⁵⁷. While common RC codes limit crack width, the presence of these cracks in elements exposed to chloride ion attack should not be overlooked. Therefore, this study considers the impact of such cracks. The cracking effect function, $f(w)$, is expressed as Eq. (4)⁵⁸, where w is the crack width (mm).

$$f(w) = 31.61w^2 + 4.73w + 1, \quad w \geq 0.1 \text{ mm} \quad (4)$$

A prediction model for the chloride ion concentration on the concrete surface is proposed as Eq. (5)⁵⁹, in which A_{cs} and ε_{cs} are the model parameters and consider the uncertainty in the model.

$$C_s = A_{cs} (w/c) + \varepsilon_{cs} \quad (5)$$

The passage of chloride ions through the thickness of the cover concrete and reaching the chloride concentration to the threshold chloride causes the dissolution of the passive protective layer on the rebar in concrete and the initiation of corrosion of the rebar^{60,61}. Determining the corrosion rate is essential in the corrosion propagation stage that follows the corrosion initiation phase. Certain studies have treated the corrosion rate as constant over time^{62,63}, while others have regarded it as variable^{54,65}.

Following the initiation of corrosion, the mechanical characteristics of the concrete cross-section components begin to deteriorate over time. This includes the compressive strength of the cover concrete (unconfined) due to the expansion of corrosion products, as well as the compressive strength and ultimate strain of the core concrete (confined) due to stirrup rebar corrosion. Additionally, the diameter, yield strength, and ultimate strain of both longitudinal and stirrup rebars degrade. The deterioration models for these mechanical properties are presented as numerical and experimental models in Eqs. (6 to 16).

Steel rebar damage model due to corrosion

Once the protective alkaline layer on the rebar is removed, chloride ions cause the rebar to rust, leading to a reduction in its diameter. The reduction of steel rebar diameter, identified as the most important consequence of corrosion^{66,67}, resulting from uniform corrosion over time is expressed in Eq. (6)^{68,69}:

$$d_b(t) = \begin{cases} d_0 & t \leq T_{init} \\ d_0 - 2 \int_{T_{init}}^t \lambda(t) dt & T_{init} < t \end{cases} \quad (6)$$

where d_0 is the intact steel rebar diameter, and $\lambda(t)$ is the corrosion rate at time t . The corrosion rate is expressed as $\lambda(t) = 0.0116 i_{corr}(t)$, where $i_{corr}(t)$ is the corrosion current density at time t , which can be estimated as Eq. (7)⁶⁹:

$$i_{corr}(t) = 0.85i_{corr,0}(t - T_{init})^{-0.29} \quad t \geq T_{init} \quad (7)$$

here, $i_{corr,0}$ represents the corrosion current density at the initiation of the second stage of the corrosion progression, as defined by the empirical Eq. (8)⁶⁹:

$$i_{corr,0} = \frac{37.5(1 - w/c)^{-1.64}}{C_b} \quad \left(\frac{\mu A}{cm^2} \right) \quad (8)$$

in this context, w/c denotes the water-to-cement ratio, and C_b stands for the previously defined cover for steel rebar. The impact of corrosion on the mechanical characteristics of steel rebar can be represented over time through empirical Eq. (9) to (11)⁷⁰:

$$f_y(t) = (1 - \alpha_y X_{corr}(t)) f_{y0} \quad (9)$$

$$f_u(t) = (1 - \alpha_u X_{corr}(t)) f_{u0} \quad (10)$$

$$\varepsilon_u(t) = (1 - \alpha_1 X_{corr}(t)) \varepsilon_{u0} \quad (11)$$

where $X_{corr}(t)$ is the mass loss of steel rebar at time t , which can be represented as $X_{corr}(t) = \frac{d_0^2 - d_b^2(t)}{d_0^2} \times 100$.

The mechanical characteristics of corroded steel rebar, denoted as

$f_y(t)$, $f_u(t)$, and $\varepsilon_u(t)$ refer to the yield strength, ultimate strength, and ultimate strain at time t , respectively. f_{y0} , f_{u0} and ε_{u0} are the mechanical characteristics of the steel rebar in intact conditions. Based on the types of steel rebar (plain or ribbed) and the corrosion types (pitting or uniform), the coefficients α_y , α_u and α_1 are suggested from the results of experimental studies^{12,71}. In this study, the mentioned coefficients are assumed to be 0.005, 0.005, and 0.035, respectively^{69,72,73}.

Unconfined concrete damage model due to corrosion

Rust, a byproduct of corrosion, possesses a lower density than intact rebar. As corrosion progresses, the volume expands due to corroded rebar. The splitting tensile stresses resulting from this volume expansion of the corrosion products induce cracking, delamination, and spalling of the cover concrete surrounding the corroded rebar. The damage inflicted on unconfined concrete by corrosion products contributes to a degradation in concrete strength. The unconfined compressive strength of the cover concrete at time t , denoted as $f_c(t)$, is expressed as Eq. (12)¹³:

$$f_c(t) = \frac{f_{co}}{1 + K [\varepsilon_1(t)/\varepsilon_{co}]} \quad (12)$$

where f_{co} is the compressive strength of cover concrete at the pristine state, K is a coefficient dependent on the surface roughness and the rebar size. For medium-sized ribbed rebar, the value of K is assumed to be 0.1⁷⁴. $\varepsilon_1(t)$ is the average tensile strain of the cracked cover concrete in the transverse direction at time t , which is presented as Eq. (13) according to the crack width¹³, and ε_{co} is the compressive strain at the peak strength of uncorroded concrete.

$$\varepsilon_1(t) = 2\pi n_{bar} (\nu_{rs} - 1) \frac{x_{cp}(t)}{b_0} \quad (13)$$

in the given equation, n_{bar} represents the number of steel rebars placed in the compressive area of the cross-section, ν_{rs} is the ratio of the volumetric expansion of the corrosion product to virgin steel rebar, with a suggested value of 2⁷⁵, and b_0 is the width of the RC cross-section in the intact state. $x_{cp}(t)$ denotes the depth of corrosion attack (corrosion depth) over time, expressed as $x_{cp}(t) = \frac{d_0 - d_b(t)}{2}$.

Confined concrete damage model due to corrosion

Transverse reinforcement confines the core concrete, which improves its maximum compressive strength and increases its ultimate strain. However, if the transverse reinforcement corrodes, these mechanical properties deteriorate. The presence of corroded transverse bars contributes to the deterioration of both the peak compressive strength and ultimate compressive strain of the confined concrete. The compressive strength of confined concrete at time t , $f_{cc}(t)$, is expressed as Eq. (14)⁷⁶:

$$f_{cc}(t) = k_c(t) f_{co} \quad (14)$$

The effect of confinement on core concrete compressive strength at time t is considered using the coefficient $k_c(t)$, which is presented as Eq. (15)⁷⁶. f_{co} is the compressive strength of core concrete in the virgin state.

$$k_c(t) = 1 + \frac{\rho_s(t) f_{yh}(t)}{f_{co}} \quad (15)$$

where $\rho_s(t)$ stands for the volumetric ratio of corroded transverse steel rebars to the volume of confined (core) concrete per unit length of the RC column. $f_{yh}(t)$ is the deteriorated yield strength of transverse steel rebar at time t , obtained from Eq. (9). $\varepsilon_{cu}(t)$ signifies the ultimate compressive strain (crushing) of the confined concrete when the fracture of the first stirrup occurs, as expressed in Eq. (16)⁷⁶:

$$\varepsilon_{cu}(t) = 0.004 + 1.4 \left[\frac{\rho_s(t) f_{yh}(t) \varepsilon_{uh}(t)}{f_{cc}(t)} \right] \quad (16)$$

Using Eq. (11), $\varepsilon_{uh}(t)$ is computed to account for the degradation of transverse rebar strain, similar to $\varepsilon_{su}(t)$, at time t .

Probabilistic method

Every reliability analysis problem is characterized by two essential components: random variables and limit state function (LSF). Random variables, denoted as X , articulate the inherent uncertainty within the problem and manifest as an n -order vector. n stands for the number of variables. The limit state function, denoted as $g(X)$, establishes a failure event dependent on all random variables X . The general form of the limit state function is defined as $g(X) = R(X) - S(X)$. Failure is recognized when the demand, denoted as $S(X)$, exceeds the capacity, represented by $R(X)$. The failure probability, p_f , is mathematically expressed through an n -fold integral, as presented in Eq. (17)⁷⁷. It is worth noting that reliability methods calculate the probability associated with the occurrence of a negative value for $g(X)$.

$$p_f = \int_{g(X) \leq 0} f(X) dX \quad (17)$$

where $f(X)$ represents the probability distribution of random variables X , known as the joint probability density function (joint PDF). Typically, this integral lacks an analytical solution and necessitates numerical calculation. FORM, recognized for its efficiency and precision, is one of the methods devised to address this probabilistic integral⁷⁸.

The first-order reliability method (FORM)

The FORM method is defined by a linear approximation of the limit state function (LSF) in the standard normal space, specifically at the design point. It is imperative for the limit state function to exhibit continuity and differentiability in proximity to either the most probable point (MPP) or the design point. The first term of the Taylor expansion of LSF around the design point is expressed as $G(u) \approx \nabla G^T(u^*) (u - u^*)$, where u denotes a random variable in standard normal space. Since u^* lies on the limit state surface, therefore,

$G(u^*) = 0$. It is assumed that $\alpha = -\frac{\nabla G(u^*)}{\|\nabla G(u^*)\|}$. Then, the LSF linear approximation can be expressed as Eq. (18).

$$G(u) \approx \|\nabla G(u^*)\| (\alpha^T u^* - \alpha^T u) \approx \|\nabla G(u^*)\| (\beta - \alpha^T u) \quad (18)$$

in which $\nabla G(u) = \left[\frac{\partial G}{\partial u_1}, \dots, \frac{\partial G}{\partial u_n} \right]$ signifies the gradient vector of $G(u)$. The gradient of LSF is a vector perpendicular to the limit-state surface. The design point, indicated as u^* , is the point on the limit state surface that is nearest to the coordinate origin in the standard normal space. For the trial point, u_m , to be considered as a design point, it must satisfy two convergence criteria. Firstly, the trial point must be sufficiently close to the limit-state surface, as indicated by $\left| \frac{G(u_m)}{G_0} \right| \leq e_1$, where G_0 represents the initial value of the LSF. Secondly, the direction of the gradient vector at the design point on the limit state surface must pass through the origin of the standard normal space, denoted by $\|u_m - (\alpha_m^T u_m)\alpha_m\| \leq e_2$. The parameters e_1 and e_2 serve as convergence thresholds, usually chosen around 0.001. Upon finding the design point, the reliability index, β , is set to the length of vector u^* , which is expressed as $\beta = \alpha^{*T} u^*$. The failure probability is also defined as Eq. (19).

$$P_f \approx \Phi(-\beta) \quad (19)$$

For finding the design point, u^* , a constrained optimization problem is solved, ensuring that the point is located on the limit state surface, as expressed in the following conditional Eq.

$$u^* = \arg \min \{ \|u\| \mid G(u) = 0 \} \quad (20)$$

In Eq. (20), “ $\arg \min$ ” refers to the argument of the minimum, representing generally the set of values where the function attains its minimum. The most important part of the FORM method is to solve the optimization problem presented in Eq. (20). Several iteration algorithms were proposed to search for the design point⁷⁹. This study employs the iHL-RF algorithm for searching the design point, as proposed by Zhang and Der Kiureghian⁸⁰. For a more in-depth understanding of FORM, it is recommended to refer to the method presented by Der Kiureghian⁷⁷, which provides additional concepts and details.

This article implements the reliability analysis using the FORM method within the MATLAB program. Throughout each step of structural reliability analysis, the selected random variables are employed, and Nonlinear dynamic analyses were performed using Open System for Earthquake Engineering Simulation (OpenSees⁸¹, Version 3.5.0 (<https://opensees.berkeley.edu>)). In the ongoing research, the limit state function is implicit, and its value is computed at each trial point using the finite element analysis output of the structural model. This output encompasses parameters such as drift, deflection, and vertical natural period. Notably, the reliability analysis program code, implemented in MATLAB, exclusively incorporates the Nataf transformation from the FERUM program series⁸².

Sensitivity analysis of structure reliability

The identification of the most influential random variable among the variables can be achieved through sensitivity analysis. One approach to sensitivity analysis relies on derivatives. Therefore, the reliability index, derived with respect to the desired distribution parameter, θ (i.e., μ_i and σ_i), is expressed as Eq. (21)⁷⁷.

$$\frac{\partial \beta}{\partial \theta} = -\frac{\nabla G^T}{\|\nabla G\|} \frac{\partial u^*}{\partial \theta} \quad (21)$$

By applying the chain rule of derivative, $\frac{\partial u^*}{\partial \theta}$ is computed. This is initially derived from the probability transformation with respect to the random variable x , and subsequently from the probability density function (PDF) of the random variable concerning the probability distribution parameter, θ , (i.e., $\frac{\partial u^*}{\partial \theta} = \frac{\partial u^*}{\partial x} \frac{\partial x}{\partial \theta}$). The sensitivity vectors δ and η indicate the sensitivity of the reliability index with respect to the mean, μ , and standard deviation, σ , as expressed in Eqs. (22) and (23)⁷⁷, respectively.

$$\delta_i = \frac{\partial \beta}{\partial \mu_i} \sigma_i \quad (22)$$

$$\eta_i = \frac{\partial \beta}{\partial \sigma_i} \sigma_i \quad (23)$$

where μ_i and σ_i are the mean and standard deviation of the random variable x_i , respectively.

Numerical analysis

This section describes the structural case study and analysis procedures used to examine the effects of corrosion on the frame's response. The aim is to demonstrate how corrosion over time impacts the probability of structural failure under both seismic loads and serviceability conditions.

The studied frame is a two-dimensional portion of a three-dimensional reinforced concrete frame according to the layout in Fig. 1a, used as the support structure for a cooling tower. It is located under corrosive environmental conditions, 500 m from the Caspian Sea coast, at the UTM coordinates shown in Fig. 1b. The gravity load from the cooling tower is applied to the reinforced concrete frame.

The case-study structure is a reinforced concrete frame comprising a single bay and single story (a simple portal frame). Figure 2a shows the geometry of the frame and applied static loads. The frame was originally designed to satisfy modern building code requirements (Iranian national building code and seismic provisions), ensuring an adequate safety margin in the uncorroded condition⁸³. Figure 2b provides additional structural details, including member dimensions and reinforcement layout. The beam spans 6 m and the columns are 3 m tall, with design reinforcement ratios and concrete strength typical for an intermediate moment-resisting frame.

All members of the frame are assumed to be exposed to the same corrosive environment (marine atmosphere). However, a plastic mechanism analysis under lateral loading indicates that plastic hinges (zones of yielding and potential failure) form primarily at the column bases and beam-column joints. Therefore, corrosion damage at these critical hinge regions is expected to have the most significant impact on seismic performance. In the finite element model, special attention is given to simulating corrosion effects in these regions (reduced steel area and bond, weakened concrete).

Fiber-based finite element model

OpenSees finite element software is used to model and analyze the nonlinear behavior of the RC frame over time. A fiber-section beam-column element approach is adopted, allowing assignment of different material fibers (steel or concrete) across the cross-section and naturally capturing progressive deterioration of each material. Figure 3 depicts the fiber-based model of the frame. Beam and column members are modeled with nonlinear force-based beam-column elements (*dispBeamColumn* in OpenSees), subdivided into integration points that use fiber sections. The column section fibers include: steel reinforcement bars (modeled with the OpenSees *ReinforcingSteel* uniaxial material, which can represent steel with buckling and post-buckling behavior), unconfined cover concrete (*Concrete01* material), and confined core concrete (*ConfinedConcrete01* material). The beam section fibers consist of unconfined concrete (*Concrete01*) and longitudinal steel bars (*ReinforcingSteel*) since no transverse confinement effect is considered in the beam.

To simulate additional flexibility due to bar slip at the column-base connections, a zero-length spring element is included at the base of each column. This element captures the extra rotation occurring when the column's longitudinal bars slip within the foundation. The zero-length element is defined by duplicating the node at the column base (nodes 1, 2 for one column and 3, 4 for the other, as shown in Fig. 3) and connecting them with a spring. Initially, these coincident nodes are fully constrained together. Once the force in the spring reaches the slip threshold, it allows relative rotation, thereby modeling the bar-slip effect.

For material behavior, established models are incorporated to capture important failure modes:

- **Rebar buckling:** Compressive buckling of longitudinal bars is modeled via the Dhakal–Maekawa⁸⁴ model implemented within the *ReinforcingSteel* material. This model, along with the Gomes–Appleton⁸⁵ parameters, ensures that when steel experiences cyclic loading, longitudinal bars in compression can lose strength and stiffness after a certain deformation.
- **Bond slip in plastic hinges:** Within the zero-length spring at the column base, steel fibers are modeled with the *Bond_SP01* material to represent the bond stress–slip relationship of anchored bars. This helps simulate stiffness degradation due to bond deterioration, which can be exacerbated by corrosion.
- **Concrete cyclic behavior:** *Concrete01* material is used for the zero-length element's cross-section, providing a more detailed cyclic response for concrete including unloading/reloading stiffness changes. This is especially relevant as corrosion reduces concrete strength and alters its strain capacity.

To validate the modeling approach, the simulated hysteretic response of this RC frame (under cyclic lateral loading) was compared to available experimental results for similar frames. The model reproduced key response characteristics with good accuracy, including peak strength, stiffness degradation, and energy dissipation, providing confidence in its predictive capability.

Figure 4 illustrates an additional feature of the model: the inclusion of shear springs at the top of each column (column-beam junctions). These springs, implemented with OpenSees *LimitState* material (after Elwood's model⁸⁶), are placed in series with the column elements to capture shear failure modes that might occur due to pure shear or combined flexure-shear under seismic loading. The two end nodes of each spring coincide with the beam-column joint and remain locked together until a shear failure criterion is met. If the column risks shear failure, the spring will "activate," allowing a sudden drop in lateral load resistance to simulate shear capacity loss. The shear spring model uses a shear limit curve defined by the column's nominal shear strength (calculated per ASCE 41 – 17⁸⁷ provisions) and a degradation slope for post-peak shear resistance following Elwood & Shoraka's⁸⁸ shear-friction model. A residual shear strength of 20% of the nominal capacity is assigned to the spring to avoid numerical convergence issues and represent some remaining load-carrying capacity after severe shear damage⁸⁹. The spring distinguishes between:

- **Flexure-shear failure:** If the column's flexural yielding occurs and reaches the shear deformation capacity, the spring activates and limits further drift.
- **Pure shear failure:** If shear capacity is exceeded before significant yielding, the spring triggers a sudden loss of load capacity without prior flexural yielding.

Figures 4 and 5 depict the modeled behavior for flexure-shear and pure shear failures, respectively, highlighting how the *LimitState* material transitions the column from elastic/plastic response to a degraded state once the shear limit is reached. This approach ensures the frame model can capture potential brittle failures that corrosion might induce, as corrosion of stirrups reduces shear capacity, making shear failure more likely in later years.

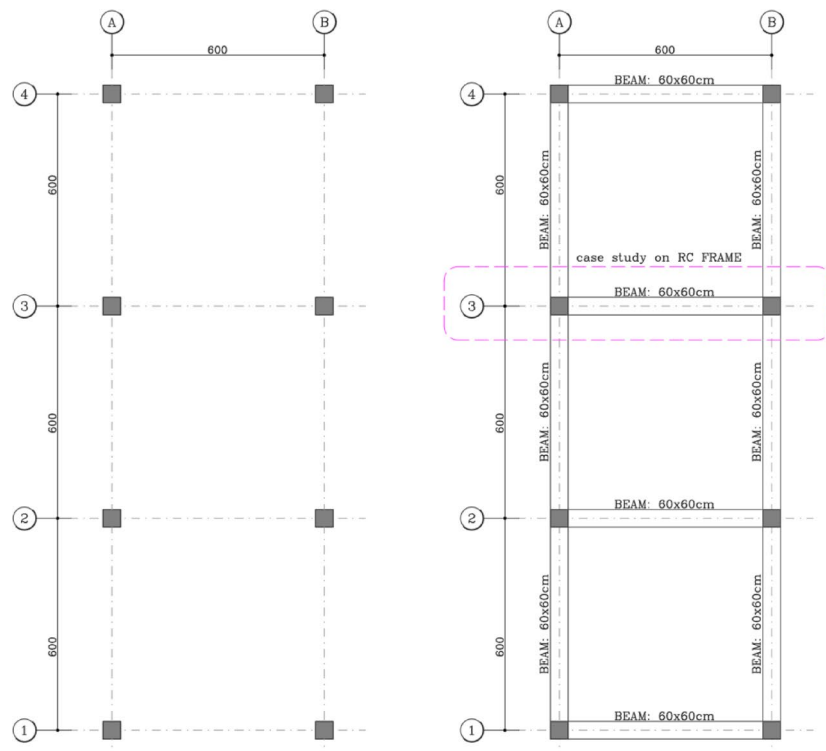


Fig. 1. (a) case study plan, (b) Location of the case study. Satellite imagery was generated using Google Earth Pro (Version 7.3.6, <https://www.google.com/earth/>). © Google.

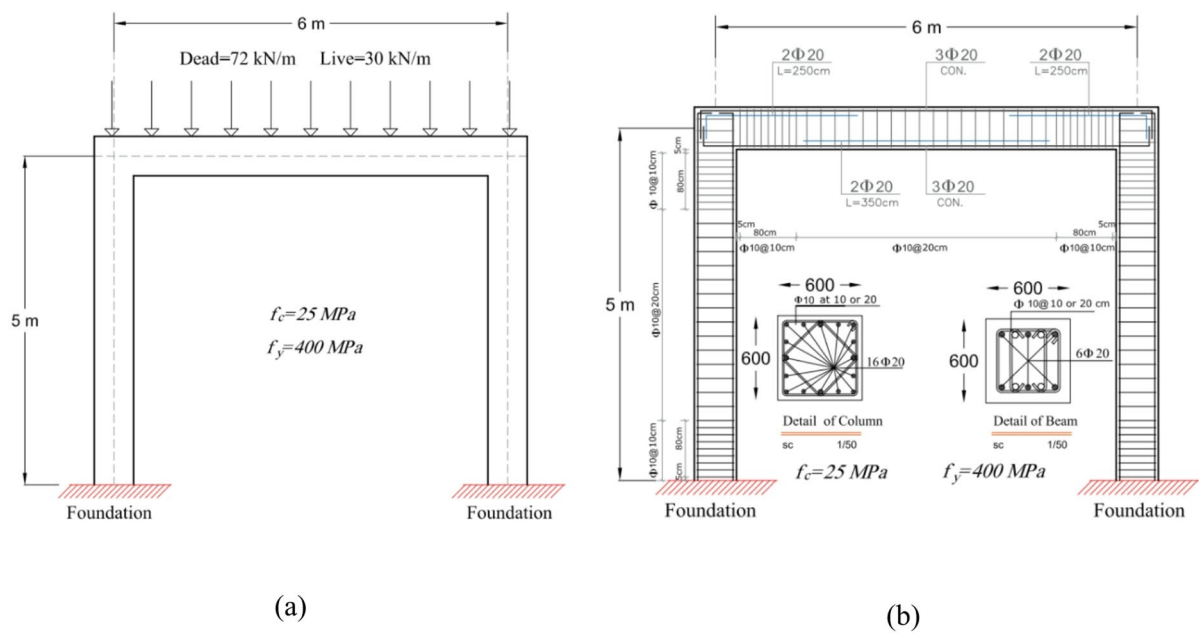


Fig. 2. (a) The Reinforced concrete frame used in this study, (b) Structural details of the case-study RC frame.

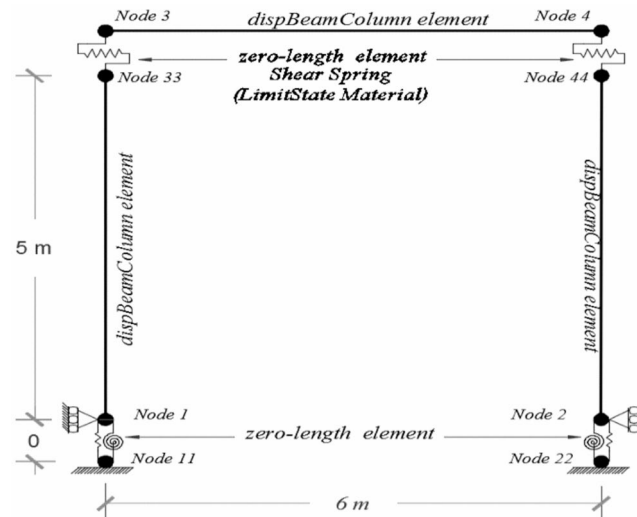


Fig. 3. A finite element model of the case-study RC frame.

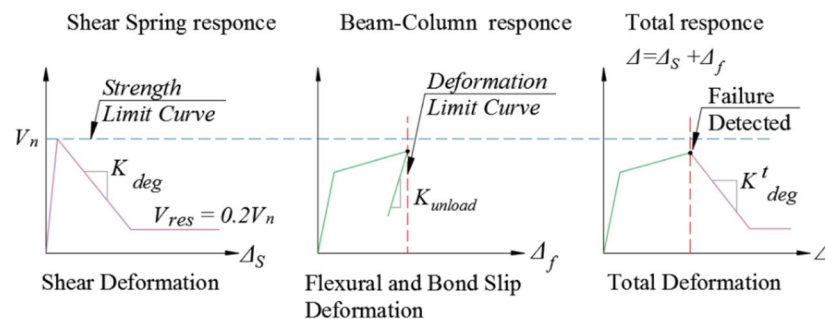


Fig. 4. Behavior model of LimitState materials in flexural-shear failure related to the shear spring in the studied RC frame.

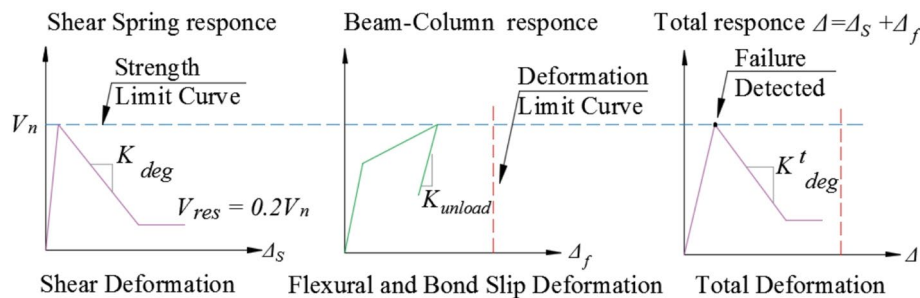


Fig. 5. Behavior model of LimitState materials in pure shear failure related to shear spring in the studied RC frame.

Parameters	Probability Distribution	Mean	Standard deviation	Unit	Refs.
<i>Random variables of concrete compressive strength</i>					
$f_{c,core}$	Lognormal	25	2.50	MPa	91,92
$f_{c,cover}$	Lognormal	25	2.50	MPa	
<i>Random variables of steel rebar</i>					
f_y	Lognormal	400	20	MPa	93
ε_{su}	Lognormal	0.15	0.0225		
d_b	Lognormal	28	1.40	mm	92
d_v	Lognormal	10	0.5	mm	92
<i>Random variables of the corrosion initiation model</i>					
D_{ref}					
w/c = 0.4	Normal	179	17.90	mm ² /year	94,95
w/c = 0.5	Normal	296	29.60	mm ² /year	94,95
C_{cr}					
0.4 = w/c	Normal	0.80	0.08	(mass% of binder)	94,95
0.5 = w/c	Normal	0.90	0.09	(mass% of binder)	94,95
A_{cs}	Normal	3.286	0.456	(mass% of binder)	94,95
ε_{cs}	Normal	0	0.384	(mass% of binder)	94,95
w_{cr}	Normal	0.30	0.03	mm	96

Table 1. Probability distribution parameters of the structure random variables.

It should be noted that the boundary conditions were idealized to some extent; therefore, any influence from neighboring elements lies outside the scope of the present analysis.⁹

Random variables

Despite many sources of uncertainty in modeling an RC frame, the focus is placed on a set of random variables representing the most influential uncertainties in corrosion and material properties. Specifically, the following parameters are treated as random variables: concrete compressive strengths (cover and core concrete), steel yield strength, steel ultimate strain, rebar diameter, cover thickness, corrosion initiation parameters C_{cr} threshold, surface chloride C_s parameters, and corrosion rate parameters. Each variable is assigned a probability distribution (often lognormal for positive-definite properties) with a specified mean and coefficient of variation based on literature. Table 1 summarizes the random variables and their statistical properties, including distribution type, mean, standard deviation, and data source.

For example, the compressive strength of cover concrete and core concrete are modeled as correlated lognormal variables (correlation coefficient 0.8 to reflect they originate from the same concrete mix⁹⁰). The mean cover concrete strength is taken as 25 MPa with 10% COV (lognormal), with similar parameters for core concrete. The diameter of longitudinal bars (25 mm nominal) and stirrup bars (10 mm) are treated as random variables to account for manufacturing tolerance and differing bar batch strengths. The mean yield strength of steel is 400 MPa (5% COV). Key corrosion model variables include the surface chloride concentration C_s (modeled via its asymptotic value parameter) and the critical threshold C_{cr} , which contain uncertainty due to environmental variability.

In addition to model parameters, seismic loading represents a major source of uncertainty. To account for variability in earthquake ground motion, a set of 11 far-field ground motion records is employed for seismic

No.	Earthquake name	Year	Station name	Component	M	Distance (Km)	PGA (g)
1	Cape Mendocino, USA	1992	Fortuna Fire	270	7.01	16.54	0.33
2	Superstition Hills, USA.	1987	Westmorland Fire	090	6.54	13.03	0.17
3	Tabas, Iran	1978	Dayhook	T1	7.35	13.94	0.41
4	Chi-Chi, Taiwan	1999	TCU045	045	7.60	77.50	0.47
5	Kobe, Japan	1995	Nishi-Akashi	000	6.90	16.20	0.50
6	Kobe, Japan	1995	Shin-Osaka	000	6.90	19.15	0.24
7	Kocaeli, Turkey	1999	Duzce	180	7.50	98.20	0.31
8	Northridge, USA.	1994	Canyon Country	000	6.70	11.39	0.41
9	Kocaeli, Turkey	1999	Ambarli	090	7.50	68.09	0.18
10	Imperial Valley, USA	1940	El Centro	180	6.90	16.40	0.32
11	Cape Mendocino, USA	1992	Rio Dell	360	7.20	10.50	0.54

Table 2. The specific properties of far-field ground motions^{97,98}.

Element type	Unconfined concrete			Confined concrete			Longitudinal reinforcement			Transverse reinforcement		
	f_{cc}	ε_{cc}	ε_{cu}	f_{cc}	ε_{cc}	ε_{cu}	f_y/f_u	ε_{sy}	ε_{su}	f_{yh}/f_{uh}	ε_{sy}	ε_{su}
	(MPa)	(%)	(%)	(MPa)	(%)	(%)	(MPa)/(MPa)	(%)	(%)	(MPa)/(MPa)	(%)	(%)
Column	RV	0.3	0.35	RV	0.3	*	R.V/R.V	R.V	R.V	R.V/R.V	R.V	R.V
Beam	R.V	0.3	0.35	RV	0.3	*	R.V/R.V	R.V	R.V	R.V/R.V	R.V	R.V

Table 3. Properties of the steel rebar and concrete. (*) According to Equation (16), it is computed as a time-dependent parameter

analysis. These records (from actual earthquakes) are selected according to FEMA P695 far-field criteria, ensuring they represent unscaled records characteristic of large events on stiff soil. Incremental Dynamic Analysis (IDA) is performed for the frame by subjecting it to each ground motion scaled to multiple intensity levels. Specifically, each accelerogram is linearly scaled to peak ground acceleration (PGA) levels of 0.1 g, 0.2 g, ..., up to 1.0 g. At each intensity, nonlinear time-history analysis is run and the structural response (e.g., peak drifts) recorded. From these analyses, the frame's limit-state exceedances (e.g., whether the frame reaches slight damage, moderate damage, etc.) are identified for each intensity and ground motion. Table 2 lists the key characteristics of the selected ground motions (event name, magnitude, distance, etc.), and Table 3 summarizes deterministic model parameters used (such as elastic modulus of concrete, which is updated with time as E_c reduces due to modulus deterioration).

The combination of random structural parameters and multiple ground motions enables building a comprehensive picture of failure probability. FORM analysis is applied for each defined limit state, implicitly integrating over the randomness in structural parameters, while the use of multiple ground motions helps in constructing probabilistic seismic demand models for fragility analysis. For the reliability calculations, seismic demand (PGA or spectral acceleration) is treated as the variable loading parameter, and ground motion variability is incorporated through the fragility curve fitting process rather than as explicit random variables in FORM (to keep the dimension of the reliability problem tractable).

Definition of limit States

Two categories of failure criteria are considered for the RC frame: (i) seismic performance criteria based on lateral drift (inter-story drift ratio) corresponding to defined damage states, and (ii) serviceability criteria based on vertical deflection and vibration comfort. Each criterion is formulated as a limit state function for reliability analysis. As discussed in Sects. "Lateral displacement criterion" and "Deflection Serviceability criterion", Δ_f represents the inter-story drift ratio under seismic loading and serves as the primary criterion for evaluating structural performance and safety, while δ_{D+L} denotes the deflection under service loads and plays a critical role in maintaining serviceability requirements and occupant comfort.

Lateral displacement criterion

In this section, failure occurs when the lateral displacement of the RC frame exceeds the allowable drift limit, defined by the limit state function $g_1(X) = \Delta_f - \Delta_X$, where Δ_f is the drift threshold for a specific damage state and Δ_X represents lateral displacement under seismic loads calculated via OpenSees. Drift thresholds are determined through pushover analysis of the intact RC frame under gravity loads, identifying critical events from the cross-sectional fiber stress-strain curve: rebar slippage, initial rebar yielding, complete rebar yielding, cover concrete spalling, and core concrete crushing. The failure mode (shear, flexural, or shear-flexural) is inferred from capacity curve degradation, as illustrated in Fig. 6, which marks these key points. Damage states are categorized into three levels: slight (exceeding drift at complete rebar yielding), moderate (exceeding drift at cover concrete spalling), and extensive (exceeding drift at core concrete crushing), as outlined in Table 4. While corrosion

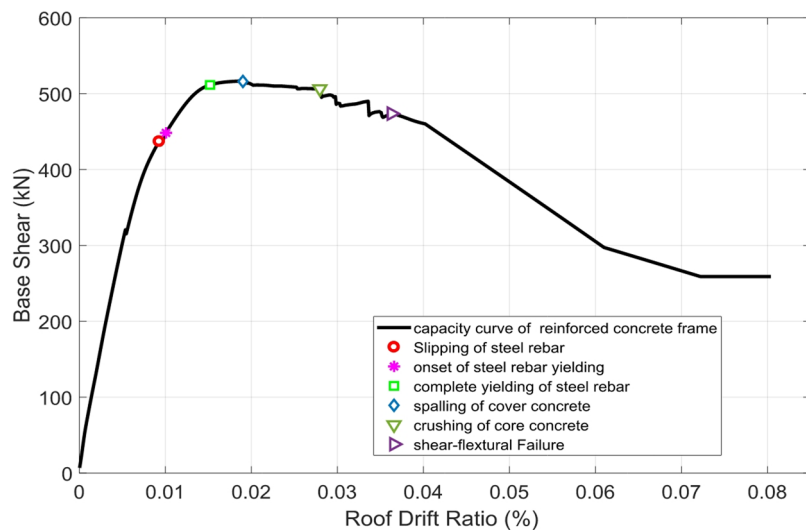


Fig. 6. The capacity curve of the case-study RC frame.

Drift threshold of damage (%)	Description	Damage state
1.520	Complete yielding of steel rebars	Slight (ds_1)
1.902	Spalling of cover concrete	Moderate (ds_2)
2.796	Crushing of core concrete	Extensive (ds_3)

Table 4. Description of case-study RC frame damage.

reduces drift thresholds in degraded structures, comparisons use intact structure thresholds to isolate corrosion-induced damage. Extensive damage, marked by core concrete crushing, does not signify total structural failure; analysis beyond this stage is omitted due to computational complexity from nonlinear dynamic behavior.

Deflection serviceability criterion

In this section, structural failure is defined as the exceedance of the mid-span immediate deflection of the beam in the RC frame under live load beyond the allowable deflection. The limit state function, g_2 , is expressed as $g_2(X) = \delta_{all} - \delta_L(X)$, where δ_{all} signifies the allowable deflection, limited to $L/360$ for live load. Here, L represents the length of the beam in the RC frame, 6 m, and $\delta_L(X)$ denotes immediate deflection as a function of all basic variables. To compute $\delta_L(X)$, the process involves first calculating the deflection caused by the dead load, denoted as $\delta_D(X)$, followed by determining the deflection due to both the dead and live loads, represented as $\delta_{D+L}(X)$. These calculations are carried out through nonlinear static analysis of the RC frame. Mathematically, this relationship is expressed as $\delta_L(X) = \delta_{D+L}(X) - \delta_D(X)$. Figure 7 shows the load-deflection curve at the mid-span of the beam in the case-study RC frame. To plot this curve, a uniform load of 0.1 kN is applied to the beam in each step. The mid-span deflection of the beam is then determined using nonlinear static analysis performed with OpenSees software. As shown in Fig. 7, the mid-span deflection of the beam under a dead load of 72 kN/m and the combined dead and live load of 102 kN/m, in the absence of corrosion effects, is 7.89 mm and 11.41 mm, respectively. Both of these values are below the allowable deflection limit.

Vibration

To ensure user comfort with the vibration, the natural frequency of the beam, f , should not fall below a certain minimum threshold. This threshold varies based on the intended use of the structure. For the purposes of this study, where the structure is assumed to be industrial, it is recommended that the vertical frequency of the case-study RC frame should not be less than 5 Hz^{99,100}.

In this section, the failure occurs when the vertical period ($T = 1/f$) of the RC frame exceeds the specified limit by 0.2 s. The limit state function is expressed as $g_3(X) = 0.2 - T_V(X)$, where $T_V(X)$ denotes the vertical period as a function of all basic variables. The vertical period of the case-study RC frame is calculated using modal analysis. Furthermore, in this study, the seismic mass along the beam length is calculated as $0.2 \times (\text{Live} + \text{Dead})$, and the dynamic elasticity modulus of concrete is assumed to be $1.25 \times E_c^{101}$.

Result and discussion

Probability of failure with the drift criterion

This section examines how chloride-induced corrosion over time affects the RC frame's seismic reliability, using lateral drift as the performance measure (as outlined in Sect. "Lateral displacement criterion"). Two corrosion

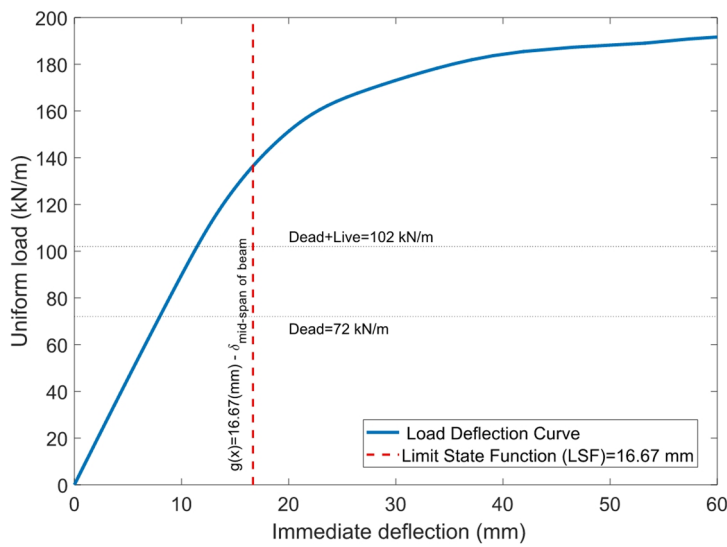


Fig. 7. The load-deflection curve of the beam of the case-study RC frame.

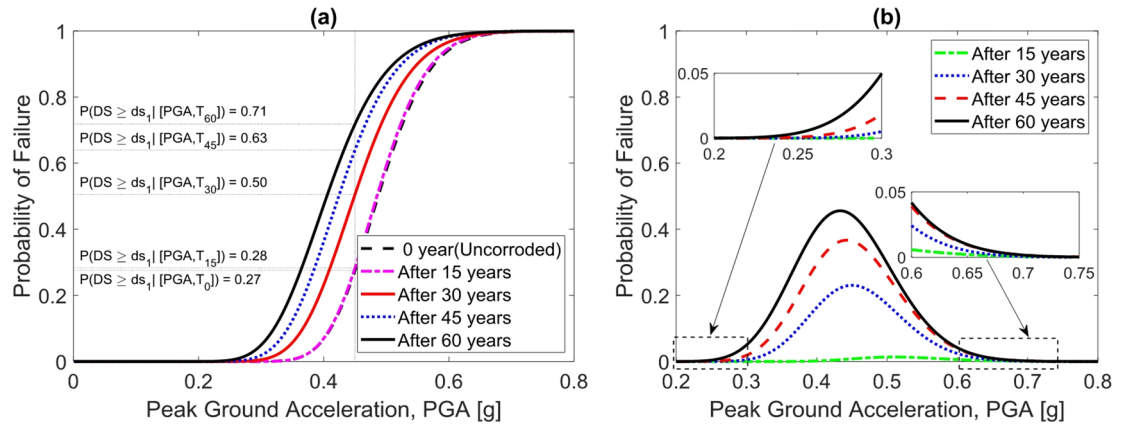


Fig. 8. Probabilistic evaluation of the case-study RC frame for ds_1 : (a) mean fragility curves, (b) difference in failure probability ($w/c=0.5$, $C_b=50$ mm, and $w_{cr}=0$ mm).

scenarios are analyzed (with identical design parameters of water–cement ratio $w/c=0.5$ and cover depth $C_b=50$ mm) that differ only in the presence of an initial crack:

- Scenario (a): Uncracked concrete cover ($w_{cr}=0$ mm) – baseline case with no initial damage.
- Scenario (b): Cracked concrete cover ($w_{cr}=0.3$ mm) – representing a realistic aggressive-environment condition where a hairline crack accelerates chloride ingress.

For each scenario, time-dependent fragility curves are computed relating earthquake intensity (PGA) to the probability of reaching or exceeding each damage state (ds_1 , ds_2 , ds_3). The fragility curves are constructed by performing FORM-based reliability analyses at multiple PGA levels. Specifically, failure probability is obtained at discrete PGA values (0.1 g increments) using the procedure described in Sect. "Random variables" (IDA results combined with reliability analysis), and then a lognormal cumulative distribution is fitted to these points. This yields a smooth fragility curve for each damage state and each time interval (0, 15, 30, 45, 60 years of corrosion).

Probabilistic analysis of corroded RC frame: scenario (a)

Figure 8a shows the fragility curves for slight damage (ds_1) at 0, 15, 30, 45, and 60 years. As expected, as corrosion progresses (moving from the "0 years" curve to "60 years"), the fragility curve shifts leftward, indicating a higher probability of reaching ds_1 for any given PGA. In other words, the structure becomes more fragile over time. For example, at a moderate earthquake intensity of $PGA=0.45$ g, the probability of at least slight damage in the uncorroded frame (0 years) is relatively low. However, after 15 years of corrosion, that probability increases to about 1.05 times the pristine value; after 30 years, 1.85 times; 45 years, 2.33 times; and by 60 years, about 2.63 times higher. This represents a dramatic increase—specifically, in the pristine state at $PGA=0.36$ g, the frame

had only $\sim 2\%$ chance of slight damage, whereas with 60-year corrosion, the chance rises to $\sim 25\%$ at the same intensity. Notably, until corrosion actually initiates (which for the parameters in this study is around 10–15 years), the fragility remains essentially unchanged; indeed the 0-year and 15-year curves nearly overlap for ds_1 , since by 15 years not enough corrosion has occurred to affect strength.

Figure 8b directly plots the difference in failure probability for ds_1 between the corroded and pristine cases at each time slice. This highlights that corrosion increases the probability of slight damage by up to $\sim 1\%$ (absolute) at 15 years, 23% at 30 years, 37% at 45 years, and 46% at 60 years (for certain PGA ranges). The largest impact of corrosion on ds_1 fragility occurs in a moderate PGA range (~ 0.2 – 0.7 g); at very high PGAs (> 0.75 g), even the intact frame is likely to experience ds_1 , so corrosion's effect becomes negligible. Similarly, at very low PGAs (< 0.2 g), both intact and corroded frames have almost zero probability of ds_1 (no damage occurs), so the curves converge.

Analogous trends are observed for moderate damage (ds_2). Figure 9a presents the mean fragility curves for ds_2 at various times. Corrosion's impact on moderate damage probability becomes evident in the PGA range of roughly 0.30 g to 0.95 g. For instance, at $PGA = 0.60$ g, the probability of reaching ds_2 in the pristine frame is quite low, but after corrosion it increases significantly. By quantifying one point: at 0.5 g PGA, the pristine frame's chance of ds_2 is $\sim 2\%$, whereas with 60-year corrosion it rises to $\sim 25\%$. In terms of ratio, at 0.5 g the failure probability with corrosion is about 2.69 times the pristine case at 60 years (and about 1.90 times at 30 years, etc.). Figure 9b (not explicitly shown here but analogous to Fig. 8b) indicates the maximum differences in ds_2 failure probability occur around $PGA \sim 0.6$ g, with corrosion adding $\sim 3\%$ at 15 years, $\sim 26\%$ at 30 years, $\sim 42\%$ at 45 years, and $\sim 52\%$ at 60 years in absolute probability. At very high intensities (> 0.95 g), both corroded and uncorroded frames are almost certain to reach ds_2 , so the effect of corrosion vanishes.

Finally, for extensive damage (ds_3), Fig. 10a shows the fragility curves over time. The corrosion influence emerges in the PGA range ~ 0.46 g to 1.4 g. At an illustrative point, $PGA = 0.84$ g, the failure probability of ds_3 in the pristine frame is low, but with corrosion it rises: the ratio of corroded to pristine failure probability is 1.04 (15 years), 1.76 (30 years), 2.08 (45 years), and 2.36 (60 years). In absolute terms, as one example, a 2% probability of ds_3 at 0.69 g in the intact frame becomes 2% probability at a lower PGA of 0.57 g after 60 years corrosion—meaning the same level of safety is achieved only at a reduced earthquake intensity. Figure 10b shows corrosion increasing ds_3 failure probability by about 2% (15 year), 19% (30 year), 28% (45 year), and 34% (60 year) at the most sensitive PGA levels (around 0.85 g).

Overall, Scenario (a) demonstrates that even without initial cracks, long-term chloride exposure can significantly undermine the seismic reliability of the RC frame. By 60 years, the frame is substantially more fragile, especially for slight and moderate damage states. Early in life (up to ~ 15 years), the effect is minor since corrosion may not have initiated or progressed much. But once corrosion becomes active, probabilities of exceeding damage states climb sharply with time.

Probabilistic analysis of corroded RC frame: scenario (b)

Scenario (b) – 0.3 mm initial crack in cover. When a crack is present, corrosion initiates earlier and advances faster (due to the higher effective diffusion). This effect is reflected in the fragility results. Figure 11a presents the fragility curves for slight damage (ds_1) at 0, 15, 30, 45, 60 years for Scenario (b). The trend resembles scenario (a) but is quantitatively more severe. For instance, at $PGA = 0.45$ g, the ratio of failure probability in 15, 30, 45, 60 years to that at 0 years is 1.92, 2.50, 2.85, 3.08, respectively. Compared to scenario (a), by 60 years the failure probability for ds_1 has increased about 3.08-fold (in scenario (b)) versus 2.63-fold (scenario (a)) at that PGA. This indicates the cracked scenario experiences a greater reduction in seismic capacity over the same time period.

Notably, at time 0, the fragility curves for scenario (a) and (b) are identical, as expected, because initially the only difference is the presence of a crack which does not affect capacity until it accelerates corrosion. At time 0, no corrosion has occurred in either scenario, so both have the same strength. The divergence appears as soon as

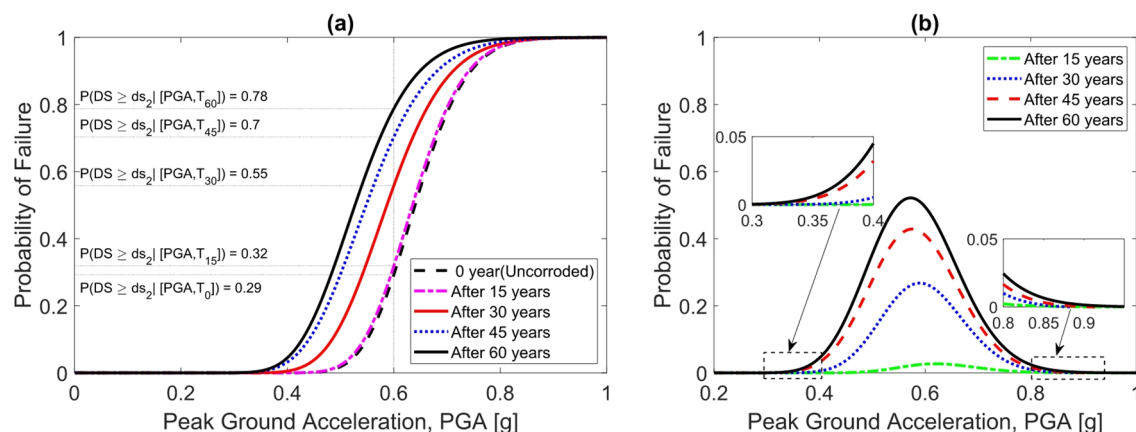


Fig. 9. Probabilistic evaluation of the case-study RC frame for ds_2 : (a) mean fragility curves, (b) difference in failure probability ($w/c = 0.5$, $C_b = 50$ mm, and $wcr = 0$ mm).

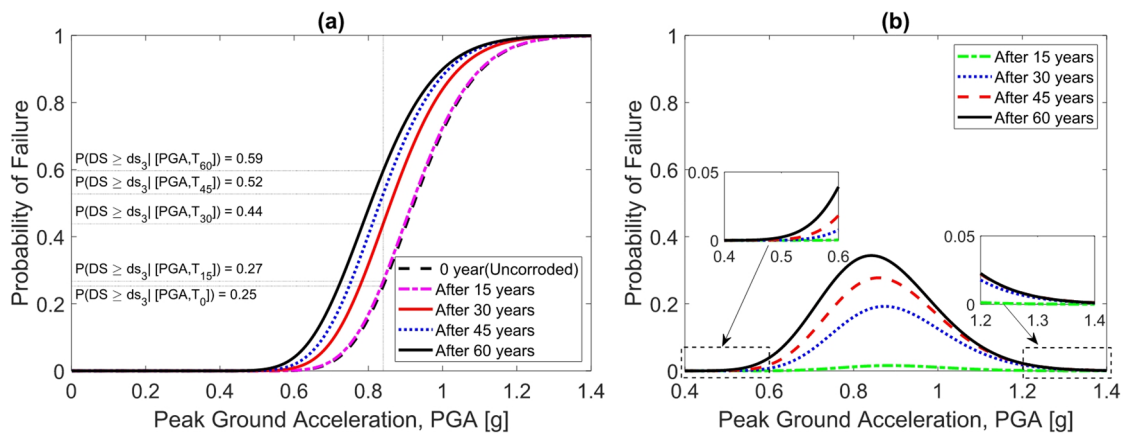


Fig. 10. Probabilistic evaluation of the case-study RC frame for ds_3 : (a) mean fragility curves, (b) difference in failure probability ($w/c=0.5$, $C_b=50$ mm, and $w_{cr}=0$ mm).

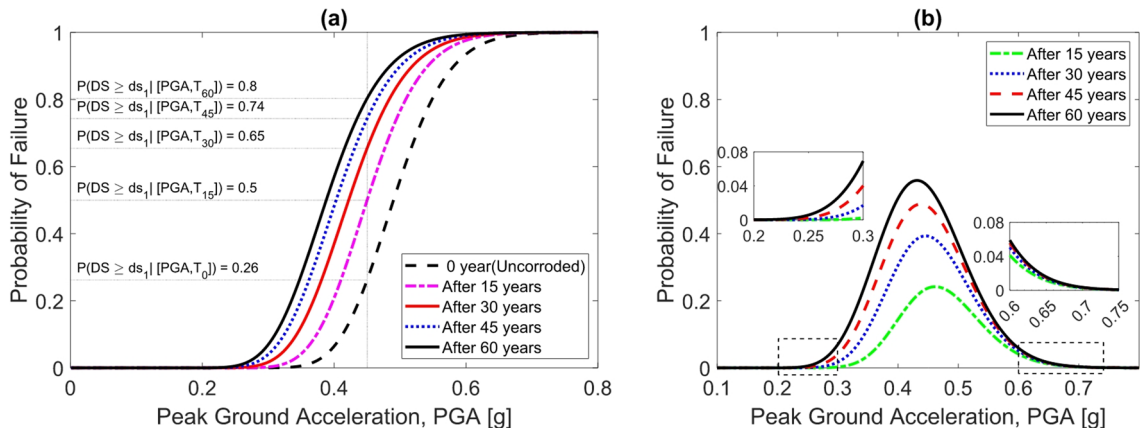


Fig. 11. Probabilistic evaluation of the case-study RC frame for ds_1 : (a) mean fragility curves, (b) difference in failure probability ($w/c=0.5$, $C_b=50$ mm, and $w_{cr}=0.3$ mm).

corrosion begins. Figure 11b shows the difference in failure probability for ds_1 between corroded and pristine states in scenario (b). By 15 years, scenario (b) has already accrued a larger increase (up to $\sim 2\%$ absolute, vs. $\sim 1\%$ in scenario (a)), and by 60 years the maximum difference is $\sim 34\%$. Comparing Fig. 8b (no crack) and Fig. 11b (crack) reveals that the presence of a crack roughly doubles the corrosion impact in early years, though in later years both scenarios converge somewhat as corrosion in scenario (a) catches up.

For moderate damage (ds_2), Fig. 12a plots fragility curves in scenario (b). The corrosion effect is noticeable across PGA 0.25–0.95 g. At PGA = 0.6 g, the failure probability ratios (corroded vs. pristine) are 1.97, 2.41, 2.65, 2.76 for 15, 30, 45, 60 years. Notably, at PGA = 0.5 g (a moderate earthquake), the pristine frame's ds_2 failure probability ($\sim 2\%$) jumps to $\sim 45\%$ after 60 years in the cracked scenario – a dramatic reduction in safety margin. Figure 12b shows corrosion-induced differences of $\sim 28\%$, 41%, 51%, 55% in failure probability for ds_2 at the most sensitive intensities over 15–60 years. When comparing scenario (b) to (a) for ds_2 (via Fig. 8b vs. Fig. 12b), scenario (b) consistently yields higher failure probabilities sooner. For example, by 30 years scenario (b) shows a $\sim 41\%$ max increase versus $\sim 26\%$ in scenario (a); by 60 years 55% vs. 52%, respectively. This suggests that while initially the crack greatly hastens reliability degradation, eventually both scenarios trend toward a severe loss of reliability (the difference at 60 years is smaller than at 30 years).

For extensive damage (ds_3), Fig. 13a provides fragility curves in scenario (b). The influence of corrosion manifests in PGA ~ 0.42 –1.55 g. At PGA = 0.84 g, failure probability ratios are 1.88, 2.44, 2.72, 2.88 for 15, 30, 45, 60 years. In absolute terms, what was a 2% chance of collapse (ds_3) at 0.69 g in the intact frame becomes 23% with 60-year corrosion. Figure 13b shows that corrosion in scenario (b) increases ds_3 failure probability by $\sim 23\%$, 36%, 43%, 47% at those time intervals. Additionally, cracks accelerate corrosion especially in early years, so by 15 years the difference in failure probability for ds_3 is 21% higher in scenario (b) than scenario (a); this extra gap due to cracking reduces to 13% by 60 years. This aligns with the understanding that the effect of the initial crack is most pronounced in the initial decades, effectively front-loading the damage, whereas by the end of 60 years, even the uncracked scenario has accumulated significant corrosion.

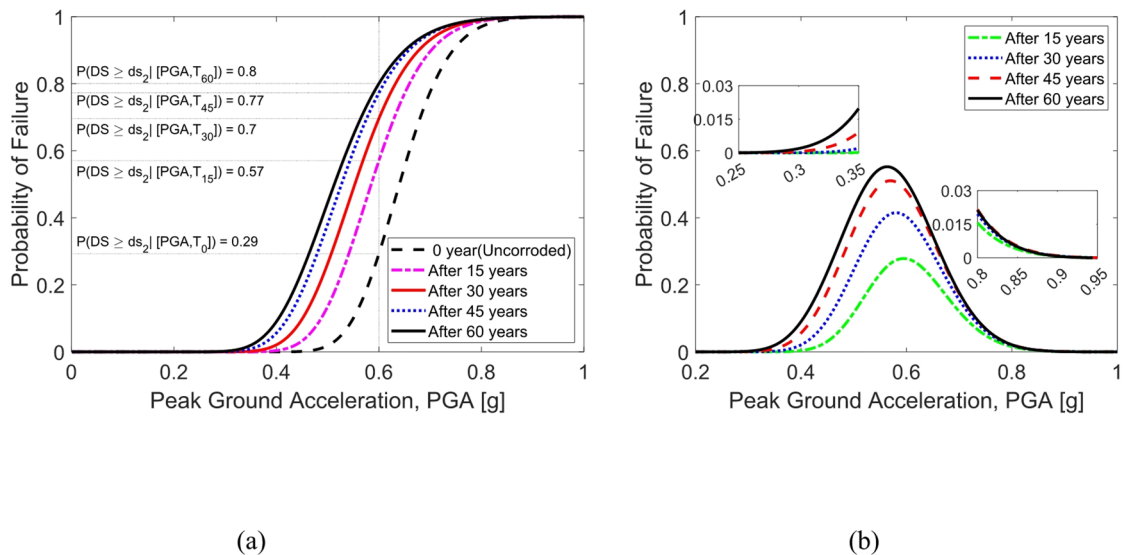


Fig. 12. Probabilistic evaluation of the case-study RC frame for ds_2 : **(a)** mean fragility curves, **(b)** difference in failure probability ($w/c = 0.5$, $C_b = 50$ mm, and $w_{cr} = 0.3$ mm).

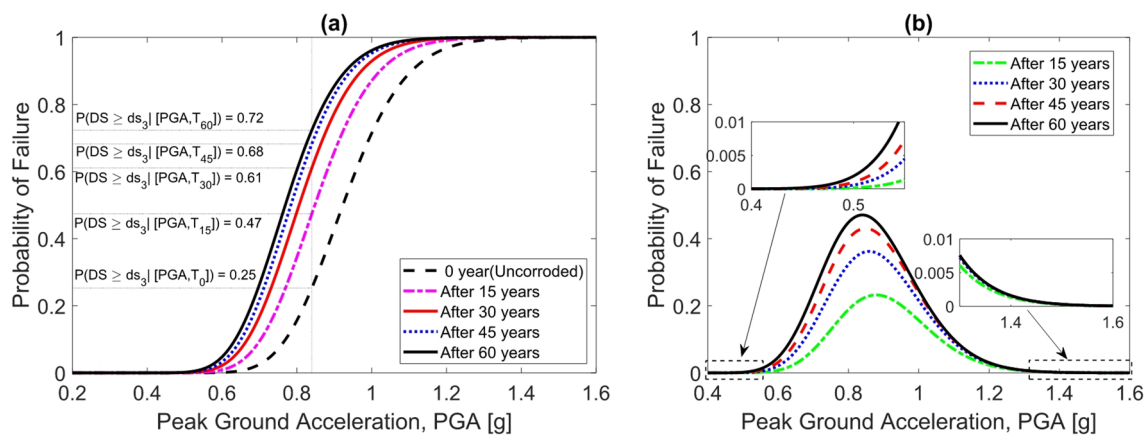


Fig. 13. Probabilistic evaluation of the case-study RC frame for ds_3 : **(a)** mean fragility curves, **(b)** difference in failure probability ($w/c = 0.5$, $C_b = 50$ mm, and $w_{cr} = 0.3$ mm).

In summary, Scenario (b) (with an initial 0.3 mm crack) shows a notably faster and greater increase in seismic fragility. Across all damage states, the cracked frame exhibits higher failure probabilities at earlier time points compared to the uncracked frame. By 60 years, scenario (b) yields roughly a $3.08\times$ increase in slight-damage failure probability (vs. pristine) while scenario (a) was $\sim 2.63\times$; for moderate and extensive damage states the cracked scenario similarly has a somewhat higher multiplier. The presence of cracks essentially accelerates the time to reach a given reliability loss. This highlights the critical importance of crack control in corrosive environments: even fine cracks can substantially reduce long-term seismic safety by enabling quicker corrosion penetration.

Failure probability due to corrosion with the serviceability criteria

The serviceability reliability of the frame is now examined, specifically analyzing deflection and vibration criteria as defined in Sects. "Deflection Serviceability criterion" and "Vibration". The analysis evaluates how the probability of exceeding serviceability limits increases with time due to corrosion. Figure 14a presents the fragility curve for the beam deflection limit state over a 60-year period. This curve illustrates the probability that the mid-span deflection under design live load will exceed the allowable limit ($L/360$) as a function of time. In scenario (a) (no initial crack) and scenario (b) (with crack), the failure probability begins at zero (at time 0, the frame satisfies deflection criteria) and increases gradually. By 60 years, corrosion causes approximately a 31% increase in deflection-failure probability for case (a) and 34% for case (b). In practical terms, the frame which originally exhibited negligible probability of unacceptable deflection acquires a moderate probability ($\sim 0.3\text{--}0.4$) of exceeding the deflection limit after decades of corrosion. The slight difference between cases (a)

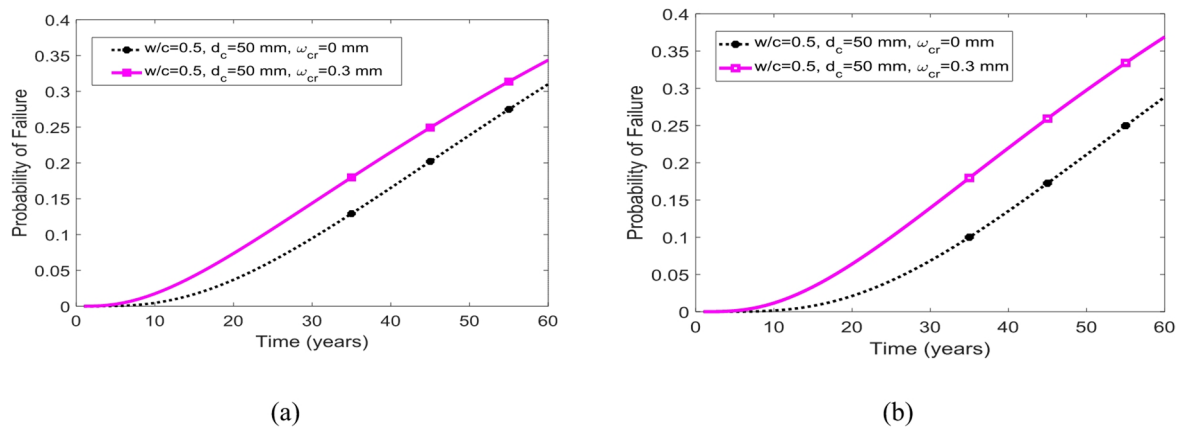


Fig. 14. Probabilistic evaluation of the case-study RC frame for **a**: deflection, **b**: vibration.

and (b) indicates that cracking (scenario b) has a marginally higher impact on deflection reliability, but both are of similar magnitude. This occurs because deflection is governed by overall stiffness loss, which depends on corrosion of both longitudinal bars and concrete cracking. Even without an initial crack, corrosion will eventually induce concrete cracking and significantly reduce stiffness. The degradation mechanism for deflection can be attributed to the loss of effective moment of inertia of the beam. Corrosion in tensile steel rebars reduces their area and elastic modulus (due to micro-cracking, etc.), and corrosion in the cover concrete reduces its contribution to stiffness. As previously noted, deflection is inversely related to stiffness ($\Delta \sim 1/EI$). Thus, as EI decreases, deflections increase, making exceedance of the allowable limit more probable. This underscores that even if a structure maintains safety against collapse, it might become serviceability-deficient (excessive sagging floors) after long-term corrosion. Figure 14b shows the fragility curves for the vibration (frequency) limit state. Similarly to deflection, the failure probability (beam frequency < 5 Hz) increases over 60 years. Corrosion leads to approximately a 28% increase in vibration-failure probability for case (a) and 37% for case (b). Initially, the frame's fundamental vertical frequency substantially exceeds 5 Hz (negligible probability of failure). Over time, as corrosion reduces structural stiffness, the frequency decreases. By 60 years, both scenarios show a notable probability that $f < 5$ Hz, indicating potential occupant exposure to uncomfortable vibrations. The slightly larger effect in scenario (b) again reflects accelerated stiffness loss due to the pre-existing crack. When comparing the deflection versus vibration reliability results, both criteria are controlled by structural stiffness degradation. The analysis reveals that the probabilities of failure for deflection and for vibration remain proximate over time. This correlation is consistent with many building codes that link vibration acceptability to deflection limits (a floor exhibiting larger deflection will also demonstrate lower frequency). These results confirm this relationship: the frame approaching the deflection limit simultaneously approaches the vibration threshold. By 60 years, the failure probabilities for deflection and vibration are nearly identical (within a few percentage points). This observation holds practical significance as it suggests that ensuring compliance with deflection serviceability requirements implicitly ensures acceptable vibration performance for this case. Indeed, certain design guidelines control vibration by indirectly limiting deflection. Overall, serviceability reliability deteriorates due to corrosion, though at a somewhat slower rate than seismic performance reliability. By 60 years, the increase in failure probability (30–37%) for serviceability is moderately lower in magnitude than that for seismic damage states (which reached up to ~ 50% or more for ds_2 , ds_3). This occurs because even under severe corrosion conditions, the frame retains residual stiffness (particularly as dead load deflection represents a static criterion without dynamic amplification). Nonetheless, a structure that initially performed well within serviceability limits could demonstrate marginal or unacceptable performance over decades in a corrosive environment.

Compared to seismic performance, which exhibited up to a 55% increase in failure probability over 60 years, the deterioration in serviceability reliability is moderately lower, ranging between 28 and 37%. This indicates that while both aspects degrade with corrosion, seismic performance is more severely affected due to its dependence on lateral stiffness and dynamic response mechanisms.

Sensitivity of model random variables on the response

This section discusses which uncertain parameters have the greatest impact on the Frame's reliability, based on sensitivity analysis. The focus is on the lateral drift criterion for moderate damage (ds_2) at a representative seismic intensity (PGA = 0.6 g) in the more severe corrosion scenario (b) – i.e., including a crack. This represents a realistic situation (cracked cover, mid-range earthquake) where multiple deterioration and loading factors interplay.

Figure 15 summarizes the sensitivity of the reliability index β (or equivalently, failure probability) with respect to the means and standard deviations of the basic random variables. The analysis reveals that among all variables, the longitudinal rebar diameter is the most crucial when considering its mean value. Increasing the mean diameter (using thicker bars or assuming less section loss) significantly raises the reliability index (meaning failure probability drops). Intuitively, a larger bar diameter provides more steel area initially, so even after corrosion, capacity remains higher. Following the rebar diameter, other important variables (in order of

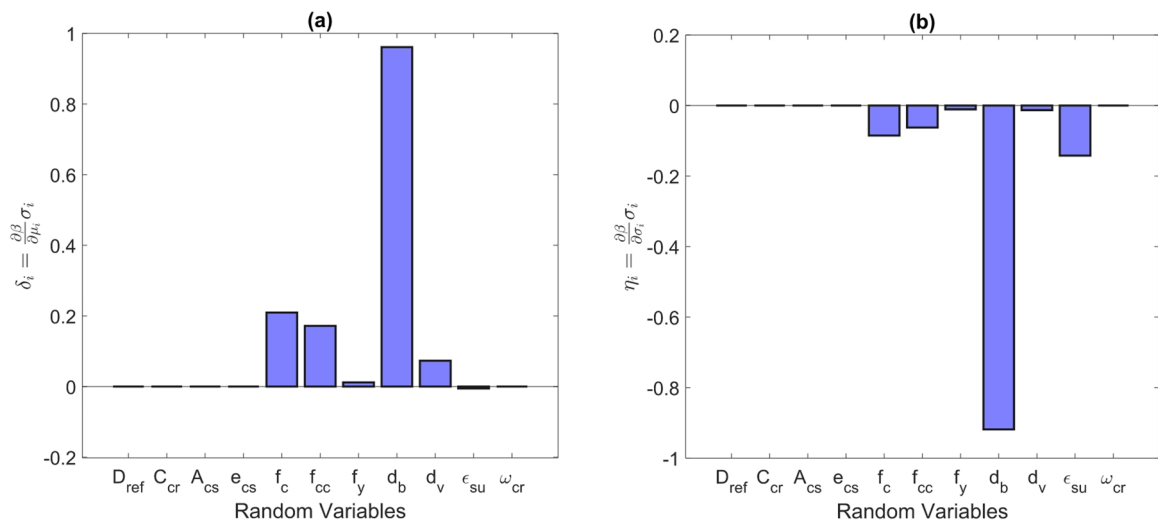


Fig. 15. Comparison of sensitivities of the variables : (a) with respect to mean; (b) with respect to standard deviation.

influence on mean) include the concrete compressive strength (cover and core) and the steel yield strength. These are capacity-side variables: higher concrete or steel strength improves drift capacity, thus reliability. On the other hand, variables related to corrosion initiation (like the threshold chloride C_{cr} or surface chloride C_s parameters) have relatively small effect on reliability by the time the structure has corroded – especially in the undamaged (initial) state. For example, at year 0 (no corrosion yet), changing C_{cr} or diffusion D doesn't affect immediate capacity. However, their importance grows as time progresses.

When considering uncertainty (standard deviation) of variables, the sensitivity analysis reveals a general trend: increasing the standard deviation of any variable decreases the reliability index. This is expected in structural reliability – more uncertainty typically means a wider spread of potential outcomes, including more in the failure tail. Figure 15b (for standard deviations) shows that this effect is fairly uniform: whether the variable is a “load” type (like corrosion rate) or a “capacity” type (like steel strength), a larger scatter leads to a heavier tail on the failure side. It is notable that variables with initially high importance (like bar diameter or concrete strength) also have high importance in terms of their uncertainty. Thus, controlling variability in these parameters (through quality control in materials, for example) can improve reliability.

To study how sensitivity evolves over time, Fig. 16 presents the reliability index sensitivity to the mean of each random variable at 15, 30, 45, 60 years. Early on (15 years), the corrosion has just started; interestingly, one particular variable from the corrosion initiation model stands out: the time to corrosion initiation (which is governed by factors like the diffusion coefficient D and threshold C_{cr}). The uncertainty in the effective time to initiation T_{init} plays a significant role in the 15-year reliability. A higher assumed mean T_{init} (assuming corrosion starts later) significantly increases reliability, because by 15 years corrosion potentially hasn't started at all. Conversely, by 60 years, the influence of T_{init} or related initial corrosion variables diminishes. This is because, regardless of when corrosion started, by 60 years all scenarios have corrosion ongoing; what matters more then is how fast corrosion propagated and what the remaining capacities are. At 60 years, capacity variables like bar diameter and steel strength dominate the sensitivity, as they directly define the reduced capacity. The diffusion coefficient and surface chloride still matter, but less so, because even slower diffusion would have led to substantial corrosion in six decades. In summary, early in the service life, uncertainty in corrosion initiation is critical, whereas later in life, the variability in residual capacity (due to both initial design parameters and corrosion progression) governs reliability.

Another insight from Fig. 16 is that as time increases, the absolute reliability index β drops. Correspondingly, the sensitivity to different variables shifts: some variables switch roles from being “load-like” to “capacity-like.” An example noted in the results is the water-cement ratio parameter: initially it may act like a load variable (a higher w/c leads to faster corrosion, reducing reliability), but eventually it can influence capacity as well (through concrete strength). By 60 years, its effect might even invert if the structure is so damaged that additional corrosion doesn't change the outcome. Overall, the sensitivity analysis underscores a few practical points:

- Robust design parameters (like using larger diameter bars or higher quality concrete) can significantly improve long-term reliability in corrosive environments, as they provide more buffer against deterioration.
- Reducing uncertainty in key variables (through better characterization or conservative design values) will improve reliability. For example, ensuring consistent concrete quality (lower COV of f_c) or using protected steel (to reduce variability in corrosion rates) can narrow the distribution of outcomes.
- In the short term, efforts to increase the corrosion initiation time (using corrosion inhibitors, better concrete cover, crack prevention) are highly effective at preserving reliability, since delaying corrosion by even a decade yields big benefits. In the long term, maintaining capacity (through maintenance, sectional enlargement or bar replacement) becomes important as those initial protections get surpassed.

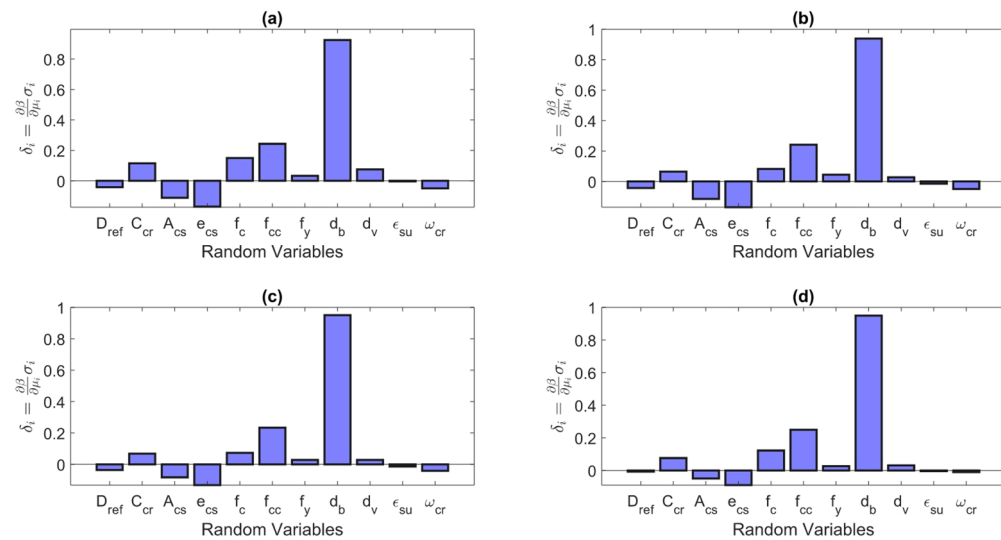


Fig. 16. Comparison of sensitivities of the reliability index with respect to mean in (a) 15 years; (b) 30 years; (c) 45 years; and (d) 60 years.

Conclusions and insights

This study presents a probabilistic framework combining the First-Order Reliability Method with nonlinear finite element modeling to evaluate the long-term effects of chloride-induced corrosion on the reliability of reinforced concrete (RC) frames. Key findings include:

- Seismic vulnerability increases significantly over time as corrosion degrades longitudinal reinforcement, leading to up to 55% higher failure probabilities for damage states after 60 years of exposure.
- Serviceability deteriorates due to stirrup corrosion and cover cracking, with failure probabilities for deflection and vibration increasing by up to 37%.
- Concrete cracking accelerates degradation, with cracked scenarios showing up to 3× higher failure probabilities, highlighting the importance of crack prevention and timely repairs.
- Early-stage reliability is sensitive to corrosion initiation parameters (e.g., diffusion coefficient, threshold concentration), while late-stage reliability depends more on residual capacity (e.g., remaining rebar area, yield strength).
- Larger rebar diameters and high material quality improve reliability, while variability in material properties consistently reduces it.
- The model's limitations include assumptions of uniform corrosion and simplified crack behavior, which may underestimate real-world deterioration patterns.

The methodology demonstrates scalability to more complex structural systems and can be further refined through future research into non-uniform corrosion mechanisms—particularly localized pitting corrosion—and time-dependent crack development. Incorporating dynamic crack opening and propagation, as well as more realistic corrosion morphologies, will improve the accuracy of long-term performance predictions and enhance the robustness of probabilistic durability models for RC structures in aggressive environments.

These results underscore the need for durability-focused design and proactive maintenance. Incorporating time-dependent reliability in design codes and implementing structural health monitoring can optimize intervention timing and extend service life. The findings of this study yield several practical recommendations to enhance durability-oriented design and maintenance strategies for RC structures in chloride-laden environments. First, crack control is essential: since cracked concrete sections demonstrated up to threefold higher failure probabilities, structural detailing should aim to limit flexural tensile stresses, maintain maximum crack widths below 0.2 mm, and consider the use of fiber reinforcement to mitigate early cracking. Second, increasing the concrete cover beyond minimum code requirements can significantly delay corrosion initiation. Third, the early phase of the service life is highly sensitive to corrosion initiation parameters, suggesting that regular inspections, at intervals of 5 to 10 years, can aid in early detection and maintenance. Finally, retrofit strategies such as externally bonded FRP, cathodic protection systems, or the use of corrosion inhibitors may help restore performance and extend the service life of aging structures. These measures are consistent with the deterioration patterns identified in this study and offer actionable guidance for improving the long-term reliability and resilience of RC frames in aggressive environments.

Future studies should explore non-uniform corrosion effects, dynamic crack growth, and corrosion-loading interactions to further improve predictive accuracy and guide the development of more resilient RC infrastructure.

Data availability

All data, models, and code generated or used during the study appear in the submitted article.

Received: 11 April 2025; Accepted: 13 October 2025

Published online: 18 November 2025

References

1. Biondini, F. & Frangopol, D. M. Time-variant redundancy and failure times of deteriorating concrete structures considering multiple limit States. *Struct. Infrastruct. Eng.* **13** (1), 94–106 (2017).
2. Ghosh, J. & Padgett, J. E. Comparative assessment of multiple deterioration mechanisms affecting the seismic fragility of aging highway bridges. *Innov. Commun. Eng.* **1**, 275 (2013).
3. Khaloo, A., Vasheghani, M. & Sedeghi, J. Contribution of water-soluble ions in the corrosion of reinforced concrete cooling towers using the response surface method. *Case Stud. Constr. Mater.* **20**, e02966 (2024).
4. Radwan, A. B., Sliem, M. H., Yusuf, N. S., Alnuaimi, N. A. & Abdullah, A. M. Enhancing the corrosion resistance of reinforcing steel under aggressive operational conditions using behentrimonium chloride. *Sci. Rep.* **9**, 18115 (2019).
5. Taheri-Shakib, J. & Al-Mayah, A. 4D evolutions of cracks, voids, and corrosion products in reinforced concrete materials. *Sci. Rep.* **13**, 22455 (2023).
6. AL-Ameeri, A. S., Rafiq, M. I. & Tsoulou, O. Combined impact of carbonation and crack width on the chloride penetration and corrosion resistance of concrete structures. *Cem. Concr. Compos.* **115**, 103819 (2021).
7. Ballarini, R. et al. *Multiple Degradation Mechanisms in Reinforced Concrete Structures, Modeling and Risk Analysis* (No. INL/EXT-20-57095-Rev000) (Idaho National Lab.(INL), 2020). Idaho Falls, ID (United States).
8. Li, K., Zheng, H., Lu, J. X., Li, W. & Poon, C. S. Role of encapsulated corrosion inhibitor on the anti-corrosion performance of reinforcing steel in lightweight concrete. *Cem. Concr. Compos.* **146**, 105388 (2024).
9. Zhu, Y., Macdonald, D. D., Yang, J., Qiu, J. & Engelhardt, G. R. Corrosion of rebar in concrete. Part II: literature survey and statistical analysis of existing data on chloride threshold. *Corros. Sci.* **185**, 109439 (2021).
10. Ghosh, J. & Padgett, J. E. Aging considerations in the development of time-dependent seismic fragility curves. *J. Struct. Eng.* **136** (12), 1497–1511 (2010).
11. Apostolopoulos, C. A., Demis, S. & Papadakis, V. G. Chloride-induced corrosion of steel reinforcement—mechanical performance and pit depth analysis. *Constr. Build. Mater.* **38**, 139–146 (2013).
12. Imperatore, S., Rinaldi, Z. & Drago, C. Degradation relationships for the mechanical properties of corroded steel rebars. *Constr. Build. Mater.* **148**, 219–230 (2017).
13. Coronelli, D. & Gambarova, P. Structural assessment of corroded reinforced concrete beams: modeling guidelines. *J. Struct. Eng.* **130** (8), 1214–1224 (2004).
14. Shekhar, S., Freddi, F., Ghosh, J. & Lad, D. Influence of corrosion on failure modes and lifetime seismic vulnerability assessment of low-ductility RC frames. *Earthq. Eng. Struct. Dynamics.* **52** (15), 5162–5184 (2023).
15. Zhou, Z., Han, M., Dong, Y. & Yu, X. Seismic resilience of corroded mid-rise reinforced concrete structures under mainshock-aftershock sequences. *Eng. Struct.* **288**, 116192 (2023).
16. Zhang, W., Liu, Y. & Yu, Q. Q. Time-dependent seismic fragility analysis of reinforced concrete columns subjected to chloride-induced corrosion. *Eng. Struct.* **302**, 117448 (2024).
17. Sagbas, G., Sheikhi, G. R., Sarikaya, K. & Deniz, D. Field reconnaissance on seismic performance and functionality of Turkish industrial facilities affected by the 2023 Kahramanmaraş earthquake sequence. *Bull. Earthq. Eng.* **22** (1), 227–254 (2024).
18. Aydogdu, H. H. & Ilki, A. Case study for a performance based rapid seismic assessment methodology (PERA2019) based on actual earthquake damages. *Bull. Earthq. Eng.* **22**, 1–35 (2024).
19. Demir, A. et al. ... Mert, N. Destructive impact of successive high magnitude earthquakes occurred in Türkiye's Kahramanmaraş on February 6, 2023. *Bull. Earthq. Eng.* **23**, 893–919 (2024).
20. Khan, M. U., Ahmad, S. & Al-Gahtani, H. J. Chloride-induced corrosion of steel in concrete: an overview on chloride diffusion and prediction of corrosion initiation time. *Int. J. Corros.* **2017**(3), 1–9 (2017).
21. Shaikh, F. U. A. Effect of cracking on corrosion of steel in concrete. *Int. J. Concrete Struct. Mater.* **12**, 1–12 (2018).
22. Mangat, P. S., Ojedokun, O. O. & Lambert, P. Chloride-initiated corrosion in alkali activated reinforced concrete. *Cem. Concr. Compos.* **115**, 103823 (2021).
23. Andisheh, K., Scott, A., Palermo, A. & Clucas, D. Influence of chloride corrosion on the effective mechanical properties of steel reinforcement. *Struct. Infrastruct. Eng.* **15** (8), 1036–1048 (2019).
24. Fu, C., Fang, D., Ye, H., Huang, L., Wang, J. Bond degradation of non-uniformly corroded steel rebars in concrete. *Engineering Structures* **226**, 111392 (2020).
25. Koulouris, K. & Apostolopoulos, C. An experimental study on effects of corrosion and stirrups spacing on bond behavior of reinforced concrete. *Metals* **10** (10), 1327 (2020).
26. Yu, A. P., Zhao, Y. L., Diwakar, K. C., Naqvi, M. W. & Hu, L. B. An experimental and numerical study of corrosion distribution dependent bond-slip relationship of reinforced concrete. *Struct.* **46**, 1268–1279 (2022).
27. Nguyen, T. K. & Nguyen, N. T. Finite element investigation of the shear performance of corroded RC deep beams without shear reinforcement. *Case Stud. Constr. Mater.* **15**, e00757 (2021).
28. Han, S. J. et al. Experimental study on shear capacity of reinforced concrete beams with corroded longitudinal reinforcement. *Materials* **12** (5), 837 (2019).
29. Ye, Z., Zhang, W. & Gu, X. Deterioration of shear behavior of corroded reinforced concrete beams. *Eng. Struct.* **168**, 708–720 (2018).
30. Xu, S., Zhang, Z., Li, R. & Qiu, B. Experimental study on the shear behavior of RC beams with corroded stirrups. *J. Adv. Concr. Technol.* **15** (4), 178–189 (2017).
31. Huang, L., Ye, H., Jin, X., Jin, N. & Xu, Z. Corrosion-induced shear performance degradation of reinforced concrete beams. *Constr. Build. Mater.* **248**, 118668 (2020).
32. Meet, S., Trishna, C. & Naveen, K. Investigating the nonlinear performance of corroded reinforced concrete beams. *J. Building Eng.* **44**, 102640 (2021).
33. Zheng, Y., Zheng, S. S., Yang, L., Dong, L. G. & Ruan, S. Experimental study and numerical model of the seismic behavior of reinforced concrete beams in an artificial corrosion environment. *J. Building Eng.* **46**, 103705 (2022).
34. Guo, A., Li, H., Ba, X., Guan, X. & Li, H. Experimental investigation on the Cyclic performance of reinforced concrete piers with chloride-induced corrosion in marine environment. *Eng. Struct.* **105**, 1–11 (2015).
35. Xu, J. G., Feng, D. C., Wu, G., Cotovos, D. M. & Lu, Y. Analytical modeling of corroded RC columns considering flexure-shear interaction for seismic performance assessment. *Bull. Earthq. Eng.* **18**, 2165–2190 (2020).
36. Lejouad, C., Richard, B., Mongabure, P., Capdevielle, S. & Ragueneau, F. Assessment of the seismic behavior of reinforced concrete elements affected by corrosion: an objective comparison between quasi-static and dynamic tests. *Struct.* **39**, 653–666 (2022).
37. Han, S. J., Ishida, T. & Tsuchiya, S. Multiscale finite element analysis of earthquake-induced damage on underground RC culverts: the role of reinforcing bar corrosion. *Struct.* **55**, 763–777 (2023).

38. Pinto, F., Astroza, R., Bazález, R. & Hernández, F. Navarro, N. Probabilistic seismic assessment of multispan RC highway bridges considering soil-structure interaction and chloride-induced corrosion. *Eng. Struct.* **301**, 117257 (2024).
39. Soraghi, A. & Huang, Q. Probabilistic modeling of reinforced concrete bond behavior considering failure mode and corrosion. *Struct. Infrastruct. Eng.* **20** (2), 263–285 (2024).
40. Dizaj, E. A., Salami, M. R. & Kashani, M. M. Seismic vulnerability analysis of irregular multi-span concrete bridges with different corrosion damage scenarios. *Soil Dyn. Earthq. Eng.* **165**, 107678 (2023).
41. Panchireddi, B. & Ghosh, J. Cumulative vulnerability assessment of highway bridges considering corrosion deterioration and repeated earthquake events. *Bull. Earthq. Earthq. eEngineering* **17**, 1603–1638 (2019).
42. Sykora, M., Holicky, M., Prieto, M. & Tanner, P. Uncertainties in resistance models for sound and corrosion-damaged RC structures according to EN 1992-1-1. *Mater. Struct.* **48**, 3415–3430 (2015).
43. Faroz, S. A., Pujari, N. N. & Ghosh, S. Reliability of a corroded RC beam based on bayesian updating of the corrosion model. *Eng. Struct.* **126**, 457–468 (2016).
44. Chateauneuf, A., Messabihia, A. & Ababneh, A. Reliability analysis of corrosion initiation in reinforced concrete structures subjected to chlorides in presence of epistemic uncertainties. *Struct. Saf.* **86**, 101976 (2020).
45. Zhang, Z. et al. Seismic performance of an innovative prefabricated Bridge pier using rapid hardening ultra-high performance concrete. *Structures* **74**, 108558 (2025).
46. Yao, Y. et al. Seismic performance of steel-PEC spliced frame beam. *J. Constr. Steel Res.* **197**, 107456 (2022).
47. Ali, A., Zhang, C., Bibi, T. & Sun, L. Experimental investigation of sliding-based isolation system with re-centering functions for seismic protection of masonry structures. *Structures* **60**, 105871 (2024).
48. Gao, D., Li, Z., Ding, C. & Yu, Z. Uniaxial tensile stress-strain constitutive relationship of 3D/4D/5D steel fiber-reinforced concrete. *Constr. Build. Mater.* **470**, 140539 (2025).
49. Long, X., Li, H., Iyela, P. M. & Kang, S. B. Predicting the bond stress-slip behavior of steel reinforcement in concrete under static and dynamic loadings by finite element, deep learning and analytical methods. *Eng. Fail. Anal.* **161**, 108312 (2024).
50. Li, J., Hu, Z., Cui, J. & Lin, G. Efficient GPU-accelerated seismic analysis strategy and scenario simulation for large-scale nuclear structure cluster-soil interaction over ten million DOFs. *Comput. Geotech.* **174**, 106583 (2024).
51. Wu, Y. et al. Research on the cross-sectional geometric parameters and rigid skeleton length of reinforced concrete arch bridges: A case study of Yelanghu Bridge. *Structures* **69**, 107423 (2024).
52. Zhang, H. et al. Fatigue behavior of high-strength steel wires considering coupled effect of multiple corrosion-pitting. *Corros. Sci.* **244**, 112633 (2025).
53. Dousti, A., Rashedinia, R., Ahmadi, B. & Shekarchi, M. Influence of exposure temperature on chloride diffusion in concretes incorporating silica fume or natural zeolite. *Constr. Build. Mater.* **49**, 393–399 (2013).
54. Dey, A. & Sil, A. Advanced corrosion-rate model for comprehensive seismic fragility assessment of chloride affected RC bridges located in the coastal region of India. *Struct.* **34**, 947–963 (2021).
55. Yu, S. & Jin, H. Modeling of the corrosion-induced crack in concrete contained transverse crack subject to chloride ion penetration. *Constr. Build. Mater.* **258**, 119645 (2020).
56. Ehlen, M. A., Thomas, M. D. & Bentz, E. C. Life-365 service life prediction modeltm version 2.0. *Concr. Int.* **31** (5), 41–46 (2009).
57. Golewski, G. L. The phenomenon of cracking in cement concretes and reinforced concrete structures: the mechanism of cracks formation, causes of their initiation, types and places of occurrence, and methods of detection—a review. *Buildings* **13**, 765 (2023).
58. Kwon, S. J., Na, U. J., Park, S. S. & Jung, S. H. Service life prediction of concrete wharves with early-aged crack: probabilistic approach for chloride diffusion. *Struct. Saf.* **31** (1), 75–83 (2009).
59. DuraCrete. Statistical quantification of the variables in the limit state functions. The European Union–BRITE EuRam III, Contract BRPR-CT95-0132, Project BE95-1347/R9. European Commission (2000).
60. Alipour, A., Shafei, B. & Shinozuka, M. Performance evaluation of deteriorating highway bridges located in high seismic areas. *J. Bridge Eng.* **16** (5), 597–611 (2011).
61. Choe, D. E., Gardoni, P., Rosowsky, D. & Haukaas, T. Seismic fragility estimates for reinforced concrete bridges subject to corrosion. *Struct. Saf.* **31** (4), 275–283 (2009).
62. Reichert, T. A., Balestra, C. E. T. & de Medeiros-Junior, R. A. Coupled model on the variation of diffusion coefficient and surface chloride concentration in reinforced concrete structures over time. *Constr. Build. Mater.* **411**, 134715 (2024).
63. Nagender, T., Parulekar, Y. M., Shinde, B., Chattopadhyay, J. & Selvam, P. Degradation assessment of corroded RC frames using in-structure response spectra from shake table tests and numerical simulation. *Bull. Earthq. Eng.* **21** (12), 5683–5715 (2023).
64. Andrade, C. Steel corrosion rates in concrete in contact to sea water. *Cem. Concr. Res.* **165**, 107085 (2023).
65. Chauhan, A., Desai, Y. M., Banerjee, S. & Sharma, U. K. 3D simulation of non-uniform corrosion induced damage in reinforced concrete exposed to real climate. *Struct.* **56**, 104852 (2023).
66. Apostolopoulos, C. A. & Papadakis, V. G. Consequences of steel corrosion on the ductility properties of reinforcement bar. *Constr. Build. Mater.* **22** (12), 2316–2324 (2008).
67. Du, Y., Clark, L. A. & Chan, A. H. Impact of reinforcement corrosion on ductile behavior of reinforced concrete beams. *ACI Struct. J.* **104** (3), 285 (2007).
68. Choe, D. E., Gardoni, P., Rosowsky, D. & Haukaas, T. Probabilistic capacity models and seismic fragility estimates for RC columns subject to corrosion. *Reliab. Eng. Syst. Saf.* **93** (3), 383–393 (2008).
69. Vu, K. A. T. & Stewart, M. G. Structural reliability of concrete bridges including improved chloride-induced corrosion models. *Struct. Saf.* **22** (4), 313–333 (2000).
70. Cairns, J., Plizzari, G. A., Du, Y., Law, D. W. & Franzoni, C. Mechanical properties of corrosion-damaged reinforcement. *ACI Mater. J.* **102** (4), 256 (2005).
71. Palsson, R. & Mirza, M. S. Mechanical response of corroded steel reinforcement of abandoned concrete Bridge. *Struct. J.* **99** (2), 157–162 (2002).
72. Kordtabar, B. & Dehestani, M. Effect of corrosion in reinforced concrete frame components on pushover behavior and ductility of frame. *Struct. Concrete.* **22** (5), 2665–2687 (2021).
73. Farahani, A., Taghaddos, H. & Shekarchi, M. Influence of repair on Corrosion-Failure modes of Square-RC columns located in tidal zone. *J. Perform. Constr. Facil.* **34** (4), 04020048 (2020).
74. Capé, M. Residual service-life assessment of existing r/c structures [ms thesis]. Gothenburg, Sweden: Chalmers University of Technology, and Milan, Italy: Milan University of Technology. (1999).
75. Li, C., Song, L., Qu, F., Li, X. & Zhao, S. Study on sectional nonuniform corrosion and bond strength of plain rebar embedded in concrete. *KSCE J. Civ. Eng.* **25** (8), 3031–3040 (2021).
76. Scott, B. D., Park, R. & Priestley, M. J. Stress-strain behavior of concrete confined by overlapping hoops at low and high strain rates. In *Journal Proceedings*. 79(1), 13–27 (1982).
77. Der Kiureghian, A. First- and second-order reliability methods. In: *Engineering Design Reliability Handbook*. Volume 14. (2005).
78. Yazdanpanah, O., Dolatshahi, K. M. & Moammer, O. Earthquake-induced economic loss Estimation of eccentrically braced frames through roof acceleration-based nonmodel approach. *J. Constr. Steel Res.* **187**, 106888 (2021).
79. Nikolaidis, E., Ghiocel, D. M. & Singhal, S. (eds) *Engineering Design Reliability Handbook* (CRC, 2004).

80. Zhang, Y. & Kiureghian, D. A. Two improved algorithms for reliability analysis. In Reliability and Optimization of Structural Systems: Proceedings of the Sixth IFIP WG7.5 working conference on reliability and optimization of structural systems. 297–304 (1995). (1994).
81. OpenSees Open System for Earthquake Engineering Simulation (Version 3.5.0) [Software]. (2023). Available from <https://openes.berkeley.edu>
82. Der Kiureghian, A., Haukaas, T. & Fujimura, K. Structural reliability software at the university of California, Berkeley. *Struct. Saf.* **28** (1–2), 44–67 (2006).
83. Iranian code of practice for seismic resistant design of buildings, standard no. 2800. 4th ed. Tehran: Road, Housing and Urban Development Research Center. (2014).
84. Dhakal, R. P. & Maekawa, K. Modeling for postyield buckling of reinforcement. *J. Struct. Eng.* **128** (9), 1139–1147 (2002).
85. Gomes, A. & Appleton, J. Nonlinear Cyclic stress-strain relationship of reinforcing bars including buckling. *Eng. Struct.* **19** (10), 822–826 (1997).
86. Elwood, K. J. Modelling failures in existing reinforced concrete columns. *Can. J. Civ. Eng.* **31** (5), 846–859 (2004).
87. American Society of Civil Engineers Seismic. *Evaluation and Retrofit of Existing Buildings*, ASCE/SEI 41–13 (American Society of Civil Engineers, 2014).
88. Baradaran Shoraka, M. & Elwood, K. J. Mechanical model for Non ductile reinforced concrete columns. *J. Earthquake Eng.* **17** (7), 937–957 (2013).
89. Jeon, J. S., Lowes, L. N., DesRoches, R. & Brilakis, I. Fragility curves for non-ductile reinforced concrete frames that exhibit different component response mechanisms. *Eng. Struct.* **85**, 127–143 (2015).
90. Li, H., Li, L., Zhou, G. & Xu, L. Time-dependent seismic fragility assessment for aging highway bridges subject to non-uniform chloride-induced corrosion. *J. Earthquake Eng.* **26** (7), 3523–3553 (2022).
91. Kulak, R. F. & Marchertas, P. V. Development of a finite element based probabilistic tool (B215) Argonne National Laboratory (2003).
92. Mirza, S. A., MacGregor, J. G. & Hatzinikolas, M. Statistical descriptions of strength of concrete. *J. Struct. Div.* **105** (6), 1021–1037 (1979).
93. Balomenos, G. P. & Pandey, M. D. Finite element reliability and sensitivity analysis of structures using the multiplicative dimensional reduction method. *Struct. Infrastruct. Eng.* **12** (12), 1553–1565 (2016).
94. Visser, J. Statistical quantification of the variables in the limit state functions: DuraCrete, probabilistic performance based durability design of concrete structures. Contract BRPR-CT95-0132, project BE95-1347, Document BE95-1347. European Commission. (2000)
95. China Engineering Construction Standardization Association Standard For Durability Assessment of Concrete Structures (CECS 220. China Construction Industry Press. Beijing, China (2007). (2007).
96. Sajedi, S. & Huang, Q. Reliability-based life-cycle-cost comparison of different corrosion management strategies. *Eng. Struct.* **186**, 52–63 (2019).
97. PEER. Peer nga database pacific earthquake engineering research center. ; (2021). Available from: <http://peer.berkeley.edu/nga/>
98. FEMA P695. Quantification of building seismic performance factors., Washington, DC. (2009).
99. Fanella, D. A. & Mota, M. *Design Guide for Vibrations of Reinforced Concrete Floor Systems: the First Design Guide Developed To Assist Structural Engineers with Vibration Analysis of Reinforced Concrete Floor Systems* (Concrete Reinforcing Steel Institute, 2014).
100. Willford, M. R., Young, P. & CEng M. *A Design Guide for Footfall Induced Vibration of Structures* (Concrete Society for The Concrete Centre, 2006).
101. Pal, P. Dynamic poisson's ratio and modulus of elasticity of Pozzolana Portland cement concrete. *Int. J. Eng. Technol. Innov.* **9** (2), 131–144 (2019).

Author contributions

Behrouz Kordabar: Conceptualization, Idea, Methodology, Investigation, Visualization, Writing – original draft, Formal analysis. Mehdi Dehestani: Conceptualization, Methodology, Supervision, Project administration, Validation, Writing - review & editing.Omid Yazdanpanah: Methodology, Data Curation, Formal analysis, Validation, Writing - review & editing. Aref Hasanzadeh: Data Curation, Methodology, Validation, Writing – review & editing.

Funding

The authors declare that no funds, grants, or other support were received during the preparation of this manuscript.

Declarations

Competing interests

The authors declare no competing interests.

Additional information

Supplementary Information The online version contains supplementary material available at <https://doi.org/10.1038/s41598-025-24197-z>.

Correspondence and requests for materials should be addressed to M.D.

Reprints and permissions information is available at www.nature.com/reprints.

Publisher's note Springer Nature remains neutral with regard to jurisdictional claims in published maps and institutional affiliations.

Open Access This article is licensed under a Creative Commons Attribution-NonCommercial-NoDerivatives 4.0 International License, which permits any non-commercial use, sharing, distribution and reproduction in any medium or format, as long as you give appropriate credit to the original author(s) and the source, provide a link to the Creative Commons licence, and indicate if you modified the licensed material. You do not have permission under this licence to share adapted material derived from this article or parts of it. The images or other third party material in this article are included in the article's Creative Commons licence, unless indicated otherwise in a credit line to the material. If material is not included in the article's Creative Commons licence and your intended use is not permitted by statutory regulation or exceeds the permitted use, you will need to obtain permission directly from the copyright holder. To view a copy of this licence, visit <http://creativecommons.org/licenses/by-nc-nd/4.0/>.

© The Author(s) 2025